2023

The simulation of elastic wave propagation in presence of void in the subsurface

Brittany Ballengee
brittany.42210@gmail.com

THE SIMULATION OF ELASTIC WAVE PROPAGATION IN PRESENCE OF VOID IN THE SUBSURFACE

A thesis submitted to
Marshall University
in partial fulfillment of
the requirements for the degree of
Master of Science
in
Mechanical Engineering
by
Brittany Ballengee
Approved by
Dr. Mehdi Esmaeilpour, Committee Chairperson
Dr. Arka Chattopadhyay
Dr. Andrew Nichols

Marshall University
August 2023

Approval of Thesis

We, the faculty supervising the work of Brittany Ballengee, affirm that the thesis, *The Simulation of Elastic Wave Propagation in Presence of Void in the Subsurface*, meets the high academic standards for original scholarship and creative work established by the Weisberg Department of Mechanical and Industrial Engineering and the College of Engineering and Computer Sciences. The work also conforms to the requirements and formatting guidelines of Marshall University. With our signatures, we approve the manuscript for publication.

Dr. Mehdi Esmaeilpour, Department of Mechanical and Industrial Engineering	Committee Chairperson	Date
	Mehdi Es	4/25/2023
Dr. Arka Chattopadhyay, Department of Civil Engineering	Committee Member	Date
		4/25/2023
Dr. Andrew Nichols, Department of Civil Engineering	Committee Member	Date
		4/25/2023

Acknowledgments

I want to acknowledge my committee chairperson Dr. Mehdi Esmaeilpour and committee members, Dr. Arka Chattopadhyay and Dr. Andrew Nichols, for their help, expertise, and guidance throughout the duration of my research. The regular weekly meetings with Dr. Esmaeilpour and Dr. Chattopadhyay produced meaningful discussions and kept me on the right track in this thesis. This work was part of the "Innovative Technologies to Search, Navigate, and Map Subterranean Unpredictable Environments" project and the "Rapid and Efficient Subterranean Mapping in Urban Settings and in Hard Rock Environments" project with the US Army Engineer Research and Development Center.

I would also like to thank my parents for their continuous support and encouragement during the research and writing process. I would not have been able to be where I am today without them.

Table of Contents

List of Tables

List of Figures

Abstract

Underground voids, whether man-made (e.g., mines and tunnels) or naturally occurring (e.g., karst terrain), can cause a variety of threats to surface activity. Therefore, it is important to be able to locate and characterize a potential void in the subsurface so that mitigating measures can be taken. In real-world environments, the subsurface properties and the existence of a void is not known, so the problem is challenging to solve. The numerical analysis conducted in this study takes a step toward understanding the seismic response with and without a void in various types of domains. The Finite Difference Method (FDM) and Finite Element Method (FEM) numerical techniques were used to analyze 1-D and 2-D seismic wave propagation for homogenous domains, layered domains, and with voids in the domain. The outputs of each numerical method were compared via their results and computational efficiency, which has not been completed in the current literature. Additionally, different void shapes were placed in the computational models to analyze each method's void detection ability.

For 1-D wave propagation, both methods produced identical results at different loading frequencies and Courant numbers. Computationally, both methods have similar run times, while FDM had a simpler implementation than FEM. In a 2-D simulation, COMSOL was used for the FEM, and the staggered-grid technique was used for the FDM. Slight dispersion was observed in all the FDM solutions, where this was attributed to the step size; however, using a smaller step size significantly increased the computational time. For a homogenous model, both methods produced similar vertical particle velocity contours and surface time histories. Computationally, FDM outperformed FEM, and due to its ease of implementation, it was recommended for homogenous wave propagation. A three-layered domain was analyzed that featured a silty clay upper layer, and two lower rock layers. Contours of vertical particle velocity displayed that the

majority of the wave remained in the upper third of the domain because of the harsh difference in material properties between the first and second layers. Additionally, a numerical model was created that consisted of the material properties obtained by ultrasonic testing. Reflections were seen in the generated seismograms but were not as visible as the ones seen in the three-layered case because the measured properties are alike and allow the wave to travel easily through the domain. After analyzing the wave propagation in a domain without a void, three void shapes were placed at the center of the domain (ellipse, circle, and square), and the resulting wave propagation was analyzed. There was minimal noise near the interface of rounded shapes in the FDM results, which was attributed to the staircase approximation used to define the shape. The surface time histories displayed reflections due to the void that were not seen in homogeneous cases. The elliptical void produced slightly more pronounced reflections because the length of the shape was larger than the circle and square. The reflections were also more easily seen in the rock domain than in soil. It was difficult locating voids in the three-layer case, but plots that computed the difference between the no-void and void case revealed that the voids did affect wave propagation. The elliptical void had the largest maximum difference of the seismograms, which occurred at the receiver closest to the void. There were differences between the subtracted plots from each method, where this was attributed to the different source incorporation. However, future studies will need to be completed to fully analyze why these plots differed between each method. Reflections from the void were more easily seen in the domain featuring the results from ultrasonic testing because of the similar rock properties that the samples shared. The elliptical void had the most perturbations compared to the square and circular voids. Overall, the FEM had longer computational times than the FDM, but both methods can successfully analyze wave propagation in the studied domains.

Chapter 1: Introduction

Seismic wave propagation occurs when there is a disturbance in a medium, whether that disturbance is from an impulse on the surface or underground from an earthquake-causing event. The propagation of seismic waves strongly depends on the material properties of the medium and the source that initiated this motion. During wave propagation in a medium, individual particles in that medium start vibrating. The propagation of waves in solid elastic mediums can be seen as time-dependent displacements. In solids that exhibit elastic properties, this wave can be considered as an elastic wave. If a material is elastic, the material will return to its original state once subjected to deformation. Rock can be considered elastic if the source applied to it is weak enough to not result in permanent deformation. In elastic mediums, seismic energy can be transmitted as surface waves and body waves. The release of seismic energy near the surface of the medium can be propagated as a body wave in the body of the medium and the other remaining part can be propagated as surface waves over the surface of the medium. Body waves include two types of waves called P-waves and S-waves, while the surface waves include two types of waves called Rayleigh waves and Love waves (see Fig.1), [1,2]. A pressure wave, known as a P-wave, compresses and expands the medium in the same direction as propagation. This is also known as the "Primary" wave since they exhibit the highest velocity compared to the others and are the first to be seen on seismograms. The P-wave, affected by both shear and bulk moduli of the elastic medium, propagates with a velocity V_P in the medium. Shear waves, known as S-waves, are perpendicular to the direction of wave propagation. S-waves travel slower than P-waves, where they are seen after the P-wave arrival on a seismogram. Shear waves propagate with a velocity V_S in the elastic medium, and they are only affected by the shear modulus of the medium. The main type of surface wave is the Rayleigh wave which propagates in an elliptical fashion, where the

amplitude of the wave motion decreases exponentially with depth [1,2]. Additionally, they are slower compared to P- and S-waves. The other type of surface wave is called a Love wave, which has a horizontal motion that is perpendicular to the direction of propagation (see Fig.1). It should be noted that near the source of wave propagation in a homogenous medium, the wave is called a spherical wave since the wavefront of a body wave propagates in a spherical shape. Figure 2 shows different parts of an elastic wave due to a normal load on a free surface. The von Schmidt wave seen in Fig.2 is a head wave.

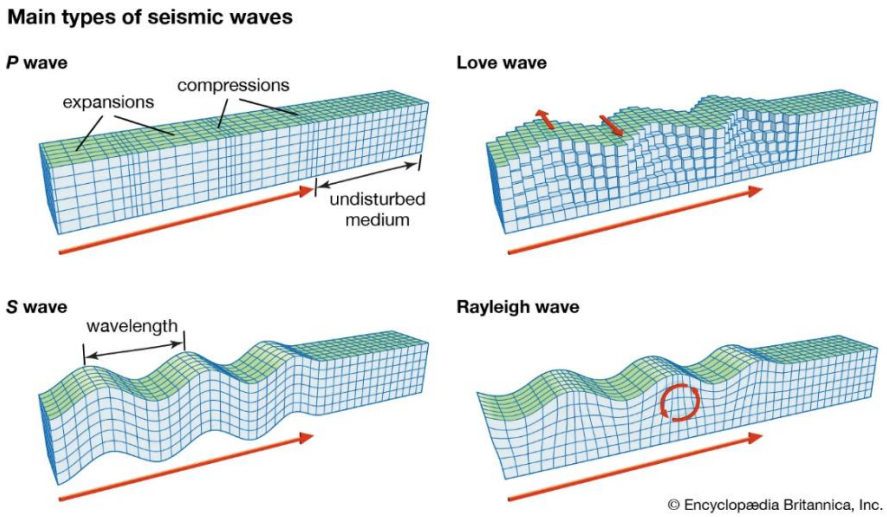

Figure 1. Body wave propagation (left) and surface wave propagation (right) in an elastic medium [2].

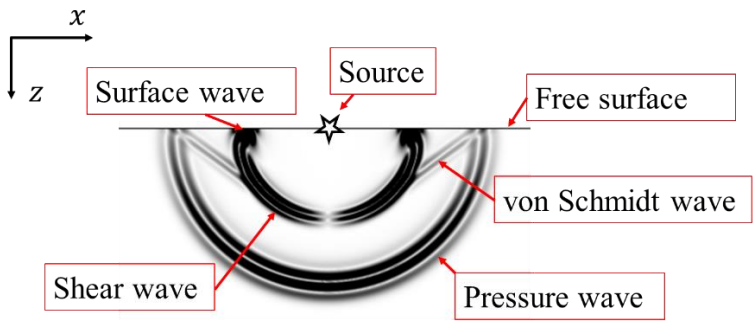

Figure 2. The structure of seismic waves due to a normal load on the free surface.

In wave propagation through a medium, the energy generated by the source is weak, and therefore the medium can be considered elastic that obeys Hooke's laws, [1]. The governing equations related to elastic wave propagation can be derived from Cauchy's equation of motion, where this equation is further discussed later in this thesis, [1]. These partial differential equations (PDEs) can be solved using both analytical and numerical methods. The common analytical methods used for solving PDEs include Laplace transforms, Fourier transforms, separation of variables, and perturbation methods. The application of these methods is limited to parameters such as the geometry of the computational domain, boundary conditions, linearity of the governing equations, and the coefficients in PDEs. Therefore, the applicability of these analytical methods is curtailed for the problem of practical interest such as wave propagation in complex domains. Therefore, numerical methods can be developed to handle the solution of PDEs with complex conditions. Different numerical methods can be used to analyze engineering problems. There are different numerical methods to solve the PDEs related to engineering problems, such as the Finite Difference Method (FDM), Finite Element Methods (FEMs), Finite Volume Method (FVM), Discontinuous Galerkin Method (DGM), Boundary Element Method (BEM), and Spectral Element Method (SEM). These methods discretize the governing equations to approximate the solution of the equations. The choice of an appropriate numerical method for solving wave propagation significantly depends on the ease of implementation, accuracy of the method, performance, and flexibility. Each of these methods has its advantages and disadvantages. The focus of this thesis is to explore both FDM and FEM methods for approximating a two-dimensional wave in the presence of a void inside the domain.

1.1 Objective of Work

Identification of the location and dimensions of voids near the subsurface is of interest to geotechnical engineers and it is controversial in the multi-layer medium due to the diffraction and reflection of waves from the layers and voids. In this thesis, two numerical methods, FDM and FEM, will be analyzed in one- and two-dimensions. Research is sparse comparing the methods, where the most notable work was from Marfurt [3] in which the accuracy of each method was compared. In this work, only a homogeneous domain was analyzed to compare the methods and did not feature layered domains or have voids near the free surface. This served as motivation for this thesis to further understand the difference between each method. The objective of this work was to understand the propagation of P-waves, S-waves, and surface waves using these two numerical methods and to study the ability of these waves in void detection in single and layered 2-D rock media. Furthermore, the quality of the solution obtained from various choices of parameters will be investigated. To be determined is an optimal numerical method that can model elastic waves with voids and layers in the computational domain. The effect of numerical analysis on model parameters and the advantages and disadvantages of using each scheme are examined in detail.

1.2 Background of Numerical Methods

The wave propagation problems in an elastic medium are of great interest in different science areas. This problem can be modeled by a set of partial differential equations with appropriate initial and boundary conditions. Numerous techniques can be employed to discretize the elastic wave equation, which is a partial differential equation that depends on the elastic parameters of the subsurface of interest. For a 1-D case, one may easily find the analytical solution for such a problem, but for 2-D domains that contain layers, surface topography, or other unique features, the

analytical solution will become difficult and tedious to solve, which is the main motivation for developing numerical solutions. Two of the most common numerical methods are the Finite Difference Method (FDM) and Finite Element Method (FEM). In the following, a brief review of using these two methods in the literature will be presented.

1.2.1 Finite Difference Method in Solving Wave Equations

In this thesis, FDM was used to simulate the propagation of elastic waves through the Earth's subsurface. The FDM is a numerical technique commonly used for various problems that approximate a solution to partial differential equations (PDEs). There are many advantages to using the FDM in solving PDEs such as high order of accuracy, low computing cost, easy implementation and robustness, and parallel computing capability. To solve the PDEs that govern elastic wave propagation, the FDM discretizes the set of equations using Taylor series expansion, where a numerical grid for time and space is defined, and then the equations are solved on nodal points. The order of accuracy depends on where Taylor's series is truncated. Depending on the arrangement of the mesh system, and the order of accuracy in space and time, there are three main grid schemes in FDM that have been applied to seismic problems, including staggered, partly-staggered, and non-staggered grid schemes (see Fig.3). According to Fig.3, in a non-staggered grid scheme all displacement (or particle-velocity), vector components are located at each grid position. In a partly-staggered scheme, the same locations are allocated to the displacement (or particle-velocity) components, however, normal and shear stress components are located at the center of the grid cell. The staggered grid has a very different scheme compared to the others in which the particle-velocity components (and/or displacement) are located at different grid positions as well as normal and shear stress components. It should be noted that each grid scheme has numerous advantages and disadvantages, which will be further discussed. The earliest classical works related

to seismic waves show the application of the FDM in solving elastic wave equations to obtain the horizontal and vertical displacement in the domain with a standard grid scheme [4-6]. Alterman and Karal [4] used the FDM to solve elastic equations of motion subjected to specific initial and boundary conditions in polar coordinates. In one work, Kelly et al. [6] used a second-order central differencing method to solve wave propagation in a domain with different layers and in the presence of free surface boundary conditions. It was found that the FDM can outperform other numerical methods and help interpret real-life seismograms.

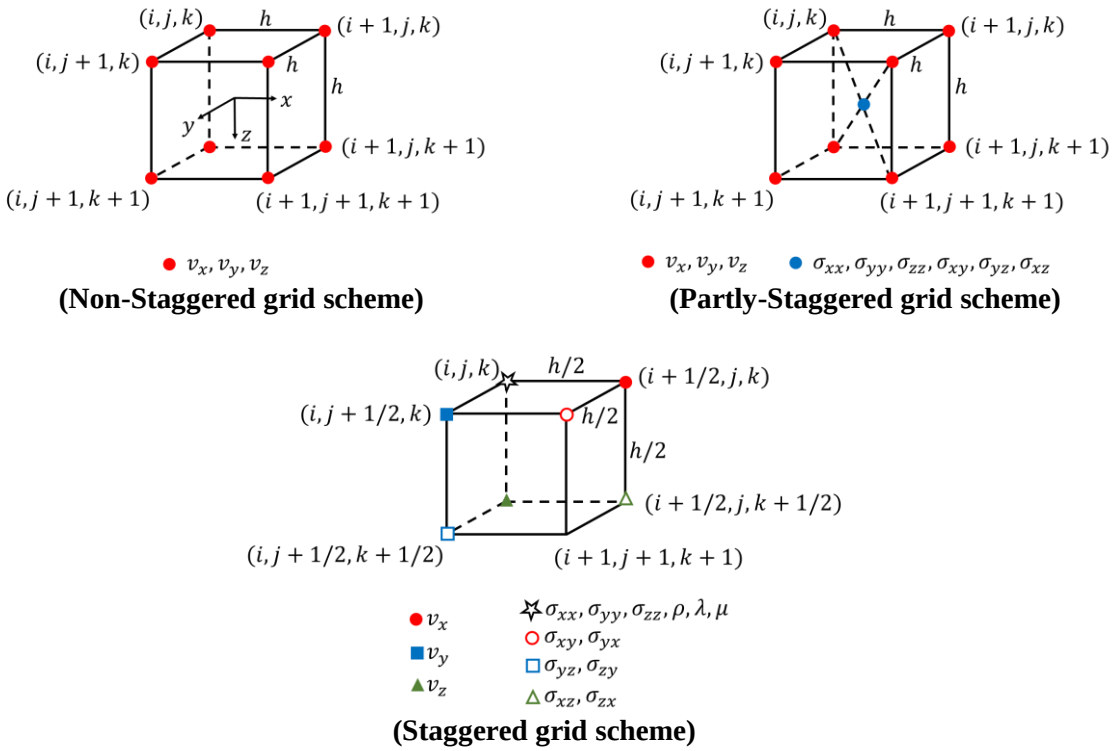

Figure 3. The grid element in non-staggered, partly-staggered, and staggered grid schemes used in FDM [7].

Due to the instability problem of the non-staggered grid in the simulation of models with high-velocity contrasts and grid dispersion in medium with slightly high Poisson's ratio [7], the staggered grid scheme was introduced by Virieux [8-9]. Since then, the staggered-grid scheme has been considered as one of the dominant schemes in the FDM simulation of elastic wave

propagation. Virieux used the velocity-stress formulation of the elastic wave equation, which is a set of 5 first-order hyperbolic equations that solve for the horizontal and vertical particle velocities, normal stresses, and tangential stress in the medium. The staggered grid scheme was later used by Levander [10] to model 2-D wave propagation and by Randall [11] and Yomogida and Etgen [12] to formulate the 3-D model of wave propagation. Levander [10] developed a 4^{th}-order finite difference staggered scheme to improve the FDM method for strong fluctuations of material properties and allowed one to model inclusions, such as cracks. It was found that, compared to 2^{nd}-order FDM schemes, using the 4^{th}-order FDM scheme in 2-D models required at least four times less memory and 3-8 times less CPU in simulation. In a series of papers, Hestholm and Ruud [13-15] used a finite-difference algorithm for both 2- and 3-D simulation of wave propagation in the presence of surface topography. A free-surface boundary condition was applied along the surface and non-reflecting absorbing boundary conditions along the edges were used in the simulation. An overview of the application of the staggered grid FDM in modeling elastic wave propagation in a 3-D medium was presented by Graves [16]. Detailed information regarding the implementation of a stable and accurate representation of a planar free-surface boundary for 3-D models and the incorporation of moment-tensor sources was presented in this work. Furthermore, the implementation of an approximate technique in simulating spatially variable anelastic attenuation was discussed. Finally, the results obtained from the staggered-grid scheme were compared with those obtained from the frequency-wavenumber algorithm, and an excellent agreement between the two methods was observed for a variety of models. Bohlen and Saenger [17] analyzed the accuracy of the staggered grid and rotated staggered grid for the modeling of Rayleigh waves. The free surface was modeled using a vacuum formulation by setting properties above the surface to zero. For a planar-free surface aligned with the grid, both methods showed good results compared

to an analytical solution. It was concluded that 15 grid points per minimum wavelength are satisfiable while modeling Rayleigh waves. For a dipping-free surface, the rotated staggered grid was more accurate but required 60 grid points per minimum wavelength. Solano et al. [18] also analyzed elastic seismic wave propagation including topography as a hill model (see Fig.4). The objective was to use the FDM on a modified staggered grid system that fitted the topography using distribution functions. Absorbing boundary conditions were used via a Conventional Perfect Matching Layer (CPML). Using the chain rule, the elastodynamic formulation was adapted on curved staggered grids. It was found that using the chain-rule approach was computationally less expensive than the tensorial approach for finite differences below the 6^{th}-order, however, it was more expensive than the classical approach for flat topography.

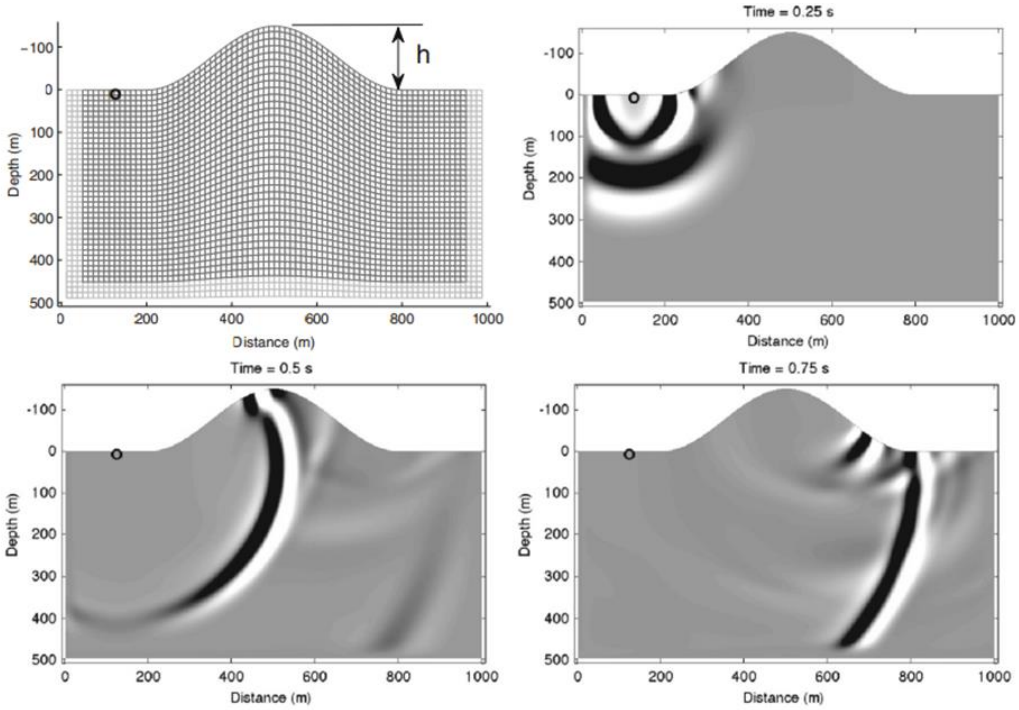

Figure 4. Snapshots of wave propagation in a hill model [18].

In the simulation of wave propagation, one important phenomenon that occurs is grid dispersion. Dispersion occurs when the phase and group velocities in the grid differ from the true velocities in the medium [19]. The velocity will depend on the sampling ratio of the spatial grid in

the finite difference formulation. The velocity will begin to vary with frequency, which will create a “tail” behind the main wave [6]. The grid-dispersion relationship of finite difference methods is found using stability analysis, which is commonly accomplished with the von Neumann method, which assumes that a plane wave propagates in the domain. This methodology is further discussed for a 1-D case.

1.2.2 Finite Element Method in Solving Wave Equation

The Finite Element Method (FEM) is another numerical technique that can be applied to model elastic wave propagation. The principle of the FEM is to discretize the computational domain into a finite number of smaller domains called elements and interpolate a solution based on the solutions in each of these elements. This is performed by deriving the weak formulation of the governing differential equations. The weak formulation of the problem is then converted to a system of ordinary differential equations which can then be solved with relative ease. There are different element shapes such as triangular or quadrilateral which will change the formulation but allows one to simulate unique topography and discontinuities more easily in the medium. In solving 3D problems, the FEM is very expensive in terms of computational resources than other numerical methods [20] since the global mass matrix must be inverted at each time step. However, it still has advantages over other methods which makes it a general tool for solving PDEs. One of the advantages of FEM is the flexibility over the discretization of the domain by giving a choice control precision at different parts of the computational domain by using proper elements. Furthermore, in FEM, different basis functions can be chosen on the elements to control the precision at computationally different parts of the domain, for instance by considering trigonometric functions instead of polynomial functions. Another advantage of the FEM is that the

free surface boundary condition is inherently satisfied. All these advantages motivate researchers to use the FEM for modeling elastic wave propagation [21-27].

Lysmer and Drake [24] is an early paper that used the FEM to model Rayleigh and Love wave propagation in a non-horizontal 2-D layered structure. The layers in the model had unique shapes, which would be difficult to model with the FDM. The goal of this work was to properly simulate earthquakes in the Central Valley in California to the Sierra Nevada. It was found that the FEM was capable of wave propagation simulation in a nonhorizontally multi-layer structure. Seron et al. [25] studied the computational aspects of the FEM for the elastic wave equation to view the accuracy, performance, and storage requirements of the method. They analyzed a homogenous model to determine which time-stepping scheme, and which iterative method was ideal for wave propagation. It was concluded that using constant average acceleration and explicit central difference along with Jacobi conjugate gradient were the most adequate integration methods and was an efficient solver. A simplified three-dimensional FEM was developed by Toshinawa and Ohmachi [26] to simulate wave propagation in 3-D sedimentary basins. The aim of this work was to model Love wave propagation in the Kanto Plain. They analyzed the effect of 3-D topography on the direction of Love-wave propagation. It was found that the 3-D simulation produced synthetics with larger amplitudes compared to the 2-D simulation and the 3-D synthetics agreed better with the observations than those from the 2-D model. Ham and Bathe [27] presented an enriched FEM to model various 2-D wave propagation problems. The proposed method combined the advantages of the FEM and spectral techniques, by preserving the fundamental properties of the FEM. The focus of the study was on the solution of problems in solids and structures using real arithmetic only. To address the numerical dispersion error in the transient wave propagation problem, the classical FEM was modified, and it is combined with the generalized gradient

smoothing technique (GGST) to handle the transient problems [28-30]. In this method, the GGST can provide softening effects to the discretized model of the structure which relieves the inherent overly stiff property of the FE method. Therefore, the stiffness of the obtained system matrices can be closer to the real system which leads to a significantly reduced numerical dispersion error in solving wave propagation problems.

Multiple commercial software programs have been developed that use finite element methods to solve a wide range of problems, including the elastic wave phenomenon. ABAQUS, ANSYS, COMSOL, plus others are commonly used. For this thesis, a code was developed in MATLAB for the simulation of elastic wave propagation in 1-D. 2-D elastic wave propagation was modeled using COMSOL Multiphysics® (COMSOL Multiphysics 6.1), a commercial software based on the FEM. The elastic wave module in COMSOL uses the discontinuous Galerkin method, which permits the use of approximating functions to be discontinuous at element interfaces and can allow for discontinuities of the media parameters.

1.3 Locating Voids Using Numerical Methods

An area of interest in seismic modeling is locating voids in the subsurface. It is important to investigate and locate a void in the Earth's subsurface because they may potentially prove problematic. A void in the subsurface could be from an underground cavity, a tunnel, or a mineshaft. The void can possibly collapse which may damage the local environment or cause bodily harm if it is located in a residential area. It is imperative to locate these voids to prevent any problems from occurring. To locate voids in the field, seismic testing is conducted by placing receivers on the surface and then applying a force on the ground, where the receivers will record the time histories (also known as a shot gather) at each point and the shot gather is then analyzed. In numerical models, the time histories can be recorded at various points in the model,

where the receivers are commonly placed on the surface. It is often helpful to create numerical models that closely represent the subsurface of interest to recognize patterns in the shot gathers that represent a potential void.

Gelis et al. [31] analyzed voids using a modified staggered grid and analyzed various void shapes filled with air. The finite-difference 2D elastic wave propagation modeling along with a Perfectly Matched Layer (PML) as an absorbing boundary condition was used in the simulation. In this work, receivers were placed on the surface and their corresponding time histories were recorded. Additionally, the phase velocity of the seismic surface waves was determined with dispersion images.

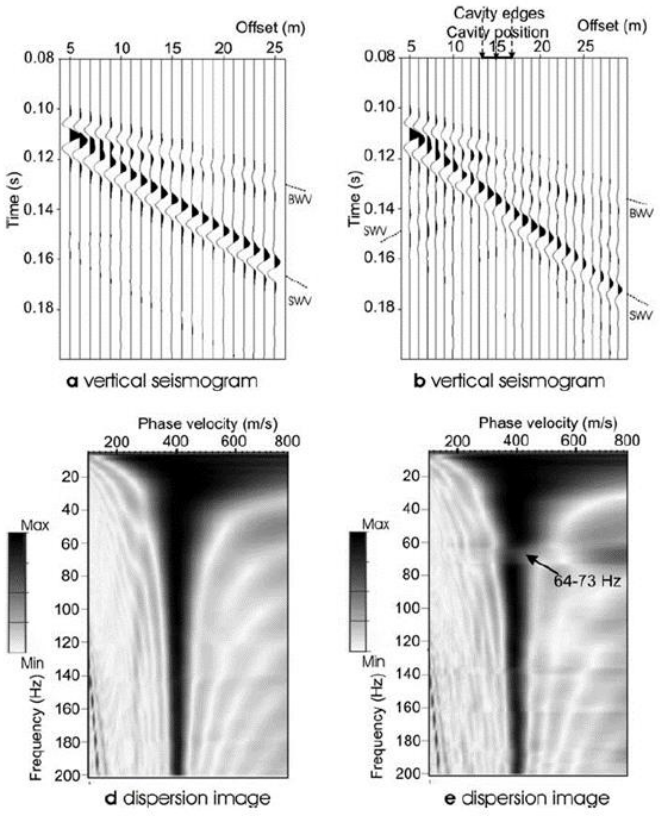

Figure 5. Results of Gelis et al. with (b and e) and without a circular void (a and d). BWV indicates Body Wave Velocity and SWV indicates Surface Wave Velocity [31].

For a circular void, Fig.5d showed the "fundamental mode of propagation with a non-dispersive phase velocity of about 400 m/s, and the loss of resolution and reduced phase velocity due to 'near-field' effects at low frequencies" [31]. In Fig.5e, there was a loss of energy for frequencies ranging from 64-74 Hz, which was not seen in the homogeneous case. This loss of energy in these specific frequency bands relates to the cavity depth, shape, and degree of modification of the surrounding medium [31]. Additionally in this work, it was found that a rectangular-shaped void generated more severe perturbations than a circular one. Lastly, a cavity surrounded by a low-velocity zone was analyzed, and it was concluded that this can possibly mask the cavity signature [31].

Schroder and Scott [32] used a 2^{nd} order FDM staggered grid to analyze elastic wave interaction with buried land mines to help in detection. The land mines were modeled as a 4cm × 8cm rectangle with a small chamber on top. Two mine types were modeled, where the chamber was air-filled or solid. The results displayed that the mine with an air-filled chamber on the top generated resonant oscillations on the surface of the mine. This resonance was attributed to trapped flexural waves between the surface and the air chamber. Jianghai et al. [33] investigated the feasibility of detecting near-surface void/fault with Rayleigh wave diffractions. In their work, an equation was developed to determine the depth to the top of a two-dimensional square void, which can be determined by the travel time data from a diffraction curve. Frequency-wave number (F-k) filtering was applied in the shot gathers to view the Rayleigh wave diffractions more clearly. Zeng et al. [34] analyzed the detectability of shallow tunnels using Rayleigh-wave diffraction, where the tunnel was modeled as a square filled with air. When decreasing the size of the tunnel, the amplitude of the Rayleigh wave diffraction also decreased. The propagation mechanisms of different waves such as P-wave, Rayleigh wave, and S-waves, and the ability of P-waves in

detecting a deep cavity in layered soil media was studied by Mirassi and Rahnema [35]. It was shown in this work that the location of the cavity could be revealed in a homogeneous half-space media using the analysis of the P-wave. Also, it was concluded that finding deep cavities using Rayleigh waves requires seismic sources with low frequencies or passive methods.

1.4 Experimental Methods to Determine Rock Properties

To create models that greater replicate the Earth's subsurface, it is important to analyze the material properties at the site of interest. Depending on the area, the properties of rock can be vastly different. The material properties can be assessed after receiving samples from a site, such as from a borehole, and can then be used in numerical models to replicate a certain site. To determine the elastic properties of rock samples, there are various experimental methods that can be applied. The properties to be determined are the P-wave velocity, S-wave velocity, and density in the medium. If these values are known, they can be incorporated into the developed numerical models. There are two types of testing methods, which are destructive and non-destructive. Destructive methods, such as a compression/tension test, will deform and potentially destroy the specimens during the testing process. The opposite of this is non-destructive, where the samples will not get damaged during the testing process. In this thesis, the focus of experimental methods is non-destructive testing, where one such method is ultrasonic testing.

1.4.1 Ultrasonic Testing of Rock Samples

The properties of a rock sample are determined by sending an ultrasonic pulse through the sample and then measuring the velocity of the pulse by knowing the time it took to reach the other end of the sample. The ultrasonic pulse velocity can then be used to find the elastic properties of the rock, estimate the location of cracks, and detect any internal abnormalities. There are three

techniques that are commonly used, which are direct pulse transmission, surface velocity measurement, and semi-direct pulse transmission [36]. Each type is seen in Fig.6.

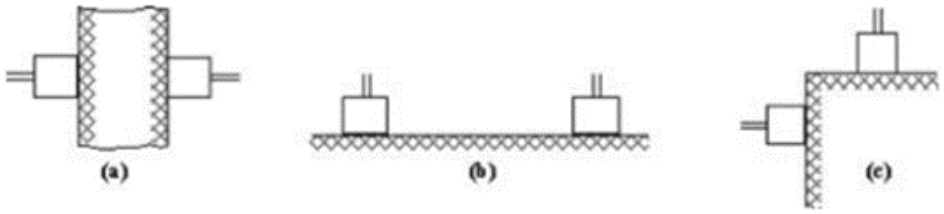

Figure 6. Pulse techniques, (a) direct transmission, (b) surface velocity measurement, and (c) semi-direct pulse transmission. [36].

Direct transmission is more commonly used compared to the others. Two transducers are placed on opposite ends of the sample and then measurements are taken. However, if the direct transmission configuration is not possible, the other two methods may need to be applied. The direct transmission technique features two transducers, which are then connected to the ultrasonic device and then to a data acquisition device, which could be a computer, to record the results. Depending on the transducer type, the P-wave and S-wave velocity of the specimen can be measured.

Basu and Aydin [36] used ultrasonic testing to characterize various rock samples that had varying compositions and weathering. They measured the P-wave velocity of the samples to evaluate a loading cell they created and to request changes to the standards of ultrasonic testing. Faim et al. [37] studied limestone samples and measured the P-wave and S-wave velocities of several specimens with varying weathering. The samples that had high weathering exhibited a lower P-wave velocity, which contributed to the attenuation of the compression wave due to the weathering. Rahmouni et al. [38] measured the P-wave velocity of calcarenite rock samples, which is a type of limestone, in both dry and saturated conditions. They determined a correlation between

P-wave velocity, porosity, and density, where equations were found from their experimental results. The equations can help predict the density and porosity of calcarenite rock.

Chapter 2: Methodology and Validations

The equations for wave propagation in an elastic medium can be derived based on the linear elasticity theory of linear elasticity by combining Hooke's law related to the definition of strain due to deformations and the equations of the relationship between stress and acceleration. The focus of this work is elastic wave equations in one dimension (1-D) and two dimensions (2-D) in elastic media.

2.1 1-D Formulation of Elastic Wave Propagation

The displacement field of an arbitrary point in the domain can be described as:

$$\rho \frac{\partial^2 u(x,t)}{\partial t^2} = E \frac{\partial^2 u(x,t)}{\partial x^2} \tag{1}$$

where $u(x,t)$ is the displacement field, E is Young's modulus, and ρ is density. The wave speed is defined as:

$$c = \sqrt{E/\rho} \tag{2}$$

Two boundary conditions and two initial conditions are needed to solve Eq. (1), which for the case of an impulse load on the left end are:

$$\begin{aligned} \frac{\partial}{\partial x} u(0,t) &= R(t) \\ u(L,t) &= 0 \\ u(x,0) &= 0 \\ \frac{\partial}{\partial t} u(x,0) &= 0 \end{aligned} \tag{3}$$

where $R(t)$ is the impulsive load and L is the length of the domain.

2.1.1 Finite Difference Formulation of the 1-D Wave Equation

The FDM difference method approximates partial differential equations using Taylor series expansions. Most used are central differencing methods, which have a higher accuracy compared

to forward and backward finite differences. A first and second derivative that is second-order accurate using central differencing is approximated as:

$$\frac{dy}{dx} = \frac{y_{i+1} - y_{i-1}}{2\Delta x} \tag{4}$$

$$\frac{d^2y}{dx^2} = \frac{y_{i-1} - 2y_i + y_{i+1}}{\Delta x^2} \tag{5}$$

where i is a grid point in space and Δx is the step size. Eq. (5) can be applied to approximate Eq. (1) as:

$$u_i^{n+1} = -u_i^{n-1} + 2u_i^n + C^2(u_{i+1}^n - 2u_i^n + u_{i-1}^n) \tag{6}$$

where i is a spatial point, n is a temporal point, and C is the Courant number defined as:

$$C = c\frac{\Delta t}{\Delta x} \tag{7}$$

This is an explicit formulation since it only solves the new time step using the previous time step's information. The stability of the scheme depends on the value of the Courant number, which should be less than or equal to 1. For layered materials with differing densities, the explicit finite difference formulation changes to:

$$u_i^{n+1} = -u_i^{n-1} + 2u_i^n + \frac{E}{\rho_i}(u_{i+1}^n - 2u_i^n + u_{i-1}^n) \tag{8}$$

The density of the material can be varied throughout the computational domain. The largest wave speed will dictate the time-step, where this indicates that in one section of the domain, the Courant number will be 1, and in others less than 1.

2.1.2 Dispersion Analysis of 1-D FDM

To analyze numerical dispersion, the work of Langtangen [39], which detailed the basics of 1-D wave propagation using the FDM, was replicated. First, a basic wave component is inserted into Eq. (6):

$$u_i^n = e^{i(kx_i - \tilde{\omega}t_n)} \tag{9}$$

where k is the wave number and $\tilde{\omega}$ is the numerical angular frequency. This will result in:

$$\sin\left(\frac{\tilde{\omega}\Delta t}{2}\right) = C\sin(\frac{k\Delta x}{2}) \tag{10}$$

where C is the Courant number. Solving for the numerical frequency leads to:

$$\tilde{\omega} = \frac{2}{\Delta t}\sin^{-1}\left(C\sin\left(\frac{k\Delta x}{2}\right)\right) \tag{11}$$

To compare numerical ($\tilde{c}$) and actual wave speed (c), the relationship between the wavenumber, speed, and angular frequency is needed which is:

$$\omega = kc \tag{12}$$

Plugging Eq. (12) into Eq. (11) turns into the relationship between numerical speed and actual wave speed as:

$$\frac{\tilde{c}}{c} = \frac{1}{Cp}\sin^{-1}(C\sin p) \tag{13}$$

where p is defined as:

$$p = \frac{k\Delta x}{2} \tag{14}$$

By plotting Eq. (13) which is presented in Fig.7, the relationship can be visualized for arbitrary values of p and C.

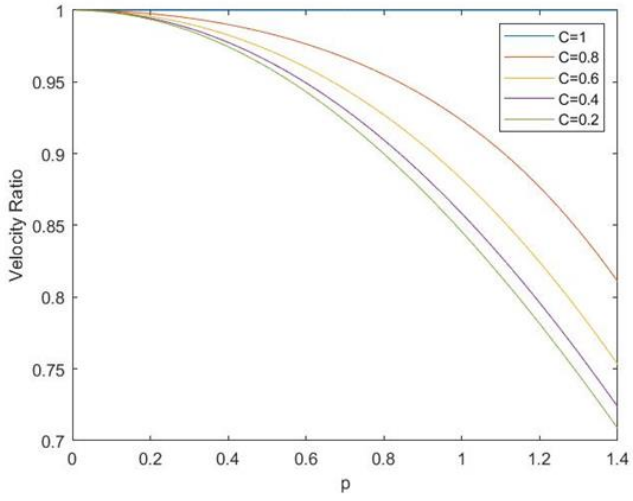

Figure 7. Numerical vs. actual wave velocity at various Courant numbers.

As seen in Fig.7, the numerical velocity will no longer be equal to the actual wave velocity due to the value of the Courant number and the spatial step size.

2.1.3 Finite Element Method of 1-D Wave Equation

The FEM discretizes the computational domain into a finite number of smaller domains called elements and interpolates a solution based on the solutions in each of these elements. This is first performed by deriving the weak formulation of the governing partial differential equation. The weak formulation of the problem is then converted to a system of ordinary differential equations which can be solved. In this work, the Galerkin formulation was used to construct the FEM formulation of the problem in 1-D.

The FEM first derives a weak form of the equation, which will turn a given partial differential equation into a restated integral form. The weak form is derived by multiplying Eq. (1) by a weight function and then integrating over the domain.

$$\int_0^l \left(\rho \ddot{u}(x,t) - E \frac{\partial^2 u(x,t)}{\partial t^2} \right) w(x) dx = 0 \tag{15}$$

$w(x)$ is the weighting function. Integrating by parts generates the following weak form:

$$\int_0^l \rho \ddot{u}\,(x,t) w(x) dx = E \left[w(x) u'(x,t)|_0^l - \int_0^l u'(x) w'(x) dx \right] \tag{16}$$

An approximation of $w(x)$ over a finite number of terms N is:

$$w_N(x) \cong \sum_{j=1}^{N} c_j \psi_j(x) \tag{17}$$

where c_j are coefficients defined by:

$$c_j = \int_0^l w(x) \psi_j(x) dx \tag{18}$$

The approximate solution $u_N(x,t)$ is:

$$u_N(x,t) \cong \sum_{i=1}^{N} d_i(t)\psi_i(t) \tag{19}$$

Inserting w_N and u_N into Eq. (16) generates the weak formulation as:

$$\rho \sum_i \sum_j \left[\int_0^l \psi_i \psi_j dx\right] \ddot{d}_i + E \sum_i \sum_j \int_0^l (\psi_i{}' \psi_j{}' dx)\, d_i = E \sum_i \sum_j \psi_j u'(x,t)\,|_0^l \tag{20}$$

which in matrix form is:

$$\boldsymbol{M}\ddot{d} + \boldsymbol{K}d = \boldsymbol{F} \tag{21}$$

where **M** is known as the mass matrix, **K** is the stiffness matrix, **F** is the load vector, and d is the nodal displacement. The basis functions used for the stiffness matrix are defined as:

$$\psi_i(x) = \begin{cases} \dfrac{x - x_{i-1}}{h_i} & for \quad x_{i-1} \le x \le x_i \\ \dfrac{x_{i+1} - x}{h_{i+1}} & for \quad x_i \le x \le x_{i+1} \\ 0 & for \quad x < x_{i-1} \ \ and \ \ x > x_{i+1} \end{cases} \tag{22}$$

where h is the size of each element.

2.2 2-D Elastic Waves: Equations of Motion

There are two different sets of equations that can be used to describe elastic wave propagation. One consists of two, second-order equations that describe the horizontal and vertical displacements in the given domain. The second type describes the motion with 5 first-order equations, which describe horizontal and vertical particle velocities, and normal and shear stresses.

2.2.1 Displacement Formulation

There are two equations of motion that derive the horizontal and vertical displacements in the medium. The equations are derived in Cartesian coordinates, where x and z are the horizontal and vertical coordinates:

$$\rho \frac{\partial^2 u}{\partial t^2} = (\lambda + 2\mu)\left(\frac{\partial^2 u}{\partial x^2} + \frac{\partial^2 w}{\partial x \partial z}\right) + \mu\left(\frac{\partial^2 u}{\partial z^2} - \frac{\partial^2 w}{\partial x \partial z}\right) \tag{23}$$

$$\rho \frac{\partial^2 w}{\partial t^2} = (\lambda + 2\mu)\left(\frac{\partial^2 u}{\partial x \partial z} + \frac{\partial^2 w}{\partial z^2}\right) + \mu\left(\frac{\partial^2 w}{\partial x^2} - \frac{\partial^2 u}{\partial x \partial z}\right) \quad (24)$$

where u and w are the horizontal and vertical displacements, λ and μ are Lamé parameters, and ρ is the density.

2.2.2 Velocity-Stress Formulation

The elastic wave equations for the 2-D case of an isotropic medium exposed to external forces (e.g., moments or body forces) can be written using a velocity-stress formulation in the form of linear and hyperbolic systems. For this formulation, there are five, hyperbolic first-order equations as:

$$\rho \frac{\partial v_x}{dt} = \frac{\partial \sigma_{xx}}{\partial x} + \frac{\partial \sigma_{xz}}{\partial z} + f_x \quad (25)$$

$$\rho \frac{\partial v_z}{dt} = \frac{\partial \sigma_{xz}}{\partial x} + \frac{\partial \sigma_{zz}}{\partial z} + f_z \quad (26)$$

$$\frac{\partial \sigma_{xx}}{\partial t} = (\lambda + 2\mu)\frac{\partial v_x}{\partial x} + \lambda \frac{\partial v_z}{\partial z} \quad (27)$$

$$\frac{\partial \sigma_{zz}}{\partial t} = (\lambda + 2\mu)\frac{\partial v_z}{\partial z} + \lambda \frac{\partial v_x}{\partial x} \quad (28)$$

$$\frac{\partial \sigma_{xz}}{\partial t} = \mu\left(\frac{\partial v_x}{\partial z} + \frac{\partial v_z}{\partial x}\right) \quad (29)$$

where the particle velocities in the x- and z- direction are denoted by v_x and v_z, respectively, compressional stress components are denoted by σ_{xx}, σ_{zz}, and the shear stress is represented by σ_{xz}. Parameters λ and μ are Lamé parameters, ρ is the density of the medium, and f_x and f_z are the space-dependent source terms in the x- and z- direction, respectively.

2.3 Finite Difference of 2-D Elastic Waves

The FDM can be applied to either type (displacement or velocity-stress) to numerically model elastic waves. The most common choice is the staggered-grid formulation. An advantage of using

the velocity-stress formulation is that it can be more readily compared to shot gathers found experimentally since in most cases, velocities at a site are recorded.

2.3.1 Standard Grid of Displacement Formulation

Using central differencing that is second-order accurate on Eqs. (23)-(24), the discretized form is:

$$u_{i,j}^{n+1} = 2u_{i,j}^{n} - u_{i,j}^{n-1} + F^2\left(u_{i+1,j}^{n} - 2u_{i,j}^{n} + u_{i-1,j}^{n}\right) + F^2(1-\gamma^2)\left(w_{i+1,j+1}^{n} - w_{i+1,j-1}^{n} - w_{i-1,j+1}^{n} + w_{i-1,j-1}^{n}\right)/4 - F^2\gamma^2\left(u_{i,j+1}^{n} - 2u_{i,j}^{n} + u_{i,j-1}^{n}\right) \tag{30}$$

$$w_{i,j}^{n+1} = 2w_{i,j}^{n} - w_{i,j}^{n-1} + F^2\left(w_{i,j+1}^{n} - 2w_{i,j}^{n} + w_{i,j-1}^{n}\right) + F^2(1-\gamma^2)\left(u_{i+1,j+1}^{n} - u_{i+1,j-1}^{n} - u_{i-1,j+1}^{n} + u_{i-1,j-1}^{n}\right)/4 - F^2\gamma^2\left(w_{i+1,j}^{n} - 2w_{i,j}^{n} + w_{i-1,j}^{n}\right) \tag{31}$$

where $x = ih$ and $z = jh$, with h being the spatial grid interval and $t = n\Delta t$ with Δt being the time-step. F is defined by the P-wave velocity, α, the time step, and the spatial step by:

$$F = \frac{\alpha \Delta t}{h} \tag{32}$$

γ is the ratio of the S-wave velocity, β, and the P-wave velocity, α,

$$\gamma = \frac{\beta}{\alpha} \tag{33}$$

where the velocities are defined by:

$$\beta = \sqrt{\mu/\rho} \tag{34}$$

$$\alpha = \sqrt{(\lambda + 2\mu)/\rho} \tag{35}$$

For the scheme to be stable, the time step must be defined as:

$$\Delta t \leq \frac{h}{(\alpha^2 + \beta^2)^{1/2}} \tag{36}$$

2.3.2 Staggered Grid of Velocity-Stress Formulation

The staggered grid formulation discretizes the velocity-stress equations. It was originally developed by Virieux [8] to simulate fluid-solid interfaces since the displacement formulation cannot accurately model these types of interfaces. The discretized form of Eqs. (27)-(29) based on a staggered grid scheme is:

$$v_{x_{i,j}}^{n+1/2} = v_{x_{i,j}}^{n-1/2} + \frac{\Delta t}{h\rho_{i+1/2,j}}\left(\sigma_{xx}{}_{i+1/2,j}^{n} - \sigma_{xx}{}_{i-\frac{1}{2},j}^{n} - \sigma_{xz}{}_{i,j+1/2}^{n} - \sigma_{xz}{}_{i,j-1/2}^{n}\right) \tag{37}$$

$$\begin{aligned} v_{z}{}_{i+1/2,j+1/2}^{n+1/2} &= v_{z}{}_{i+1/2,j+1/2}^{n-1/2} \\ &+ \frac{\Delta t}{h\rho_{i,j+1/2}}\left(\sigma_{xz}{}_{i+1,j+1/2}^{n} + \sigma_{xz}{}_{i,j+1/2}^{n} - \sigma_{zz}{}_{i+1/2,j+1}^{n} - \sigma_{zz}{}_{i+1/2,j}^{n}\right) \end{aligned} \tag{38}$$

$$\begin{aligned} \sigma_{xx}{}_{i+\frac{1}{2},j}^{n+1} &= \sigma_{xx}{}_{i+\frac{1}{2},j}^{n} + \frac{(\lambda+2\mu)_{i,j}\Delta t}{h}\left(v_{x}{}_{i+1,j}^{n+\frac{1}{2}} - v_{x}{}_{i,j}^{n+\frac{1}{2}}\right) \\ &+ \frac{\lambda_{i,j}\Delta t}{h}\left(v_{z}{}_{i+\frac{1}{2},j+1/2}^{n+1/2} - v_{z}{}_{i+\frac{1}{2},j-1/2}^{n+1/2}\right) \end{aligned} \tag{39}$$

$$\begin{aligned} \sigma_{zz}{}_{i+\frac{1}{2},j}^{n+1} &= \sigma_{zz}{}_{i+\frac{1}{2},j}^{n} + \frac{(\lambda+2\mu)_{i,j}\Delta t}{h}\left(v_{z}{}_{i+\frac{1}{2},j+\frac{1}{2}}^{n+\frac{1}{2}} - v_{z}{}_{i+\frac{1}{2},j-\frac{1}{2}}^{n+\frac{1}{2}}\right) \\ &+ \frac{\lambda_{i,j}\Delta t}{h}\left(v_{x}{}_{i+1,j}^{n+1/2} - v_{z}{}_{i,j}^{n+1/2}\right) \end{aligned} \tag{40}$$

$$\begin{aligned} \sigma_{xz}{}_{i,j+\frac{1}{2}}^{n+1} &= \sigma_{xz}{}_{i,j+\frac{1}{2}}^{n} \\ &+ \frac{\mu_{i+1/2,j+1/2}\Delta t}{h}\left(v_{z}{}_{i+1/2,j+1/2}^{n+1/2} - v_{z}{}_{i-1/2,j+1/2}^{n+1/2} + v_{x}{}_{i+1,j}^{n+1/2} - v_{x}{}_{i+1,j}^{n+1/2}\right) \end{aligned} \tag{41}$$

where i is the index for the horizontal direction, j is the index for the vertical direction, and n is the index for time. The equations were discretized by using central finite differences where the equations are verified at nodes, which created the staggered grid. With this method, the stress and

velocity are not known at the same nodal locations. Virieux [8] completed a standard spectral analysis to determine the stability condition of the staggered grid, and it was found to be:

$$\Delta t \leq \frac{h}{\sqrt{2} * v_{p,max}} \tag{42}$$

for $\Delta x = \Delta z = h$. When compared to the stability condition of the displacement formulation, this condition does not rely on the S-wave velocity of the medium.

2.4. 2-D Finite Element Methodology

COMSOL was employed to simulate elastic waves in two dimensions. For the elastic wave solvers, the discontinuous Galerkin method and a time-explicit solver are used. The variables being solved are the structural velocity components and strain components. The governing equations used in this software are:

$$\rho \frac{\partial \boldsymbol{v}}{\partial t} - \Delta \cdot \boldsymbol{S} = \boldsymbol{F}_v \tag{43}$$

$$\frac{\partial \boldsymbol{E}}{\partial t} - \frac{1}{2}[\nabla \boldsymbol{v} + (\nabla \boldsymbol{v})^T] = \boldsymbol{0} \tag{44}$$

$$\boldsymbol{S} = \boldsymbol{C} : \boldsymbol{E} \tag{45}$$

where $\boldsymbol{v}$ is velocity, $\boldsymbol{S}$ is the stress tensor, $\boldsymbol{E}$ is the strain tensor, $\boldsymbol{C}$ is the stiffness tensor, ρ is the density, and $\boldsymbol{F_v}$ is for when body force is used [40].

2.5 Boundary Conditions

There are four boundary conditions, one for each edge, which must be defined in the formulation. The simplest type is rigid boundaries, which is when the variables that are being solved for are set to zero on each edge. For an elastic wave problem, once the wave reaches a boundary, it will be reflected if there are rigid boundaries. Most often, researchers want to analyze a large space, but due to computation limitations, this may not be possible, so to simulate an infinite half-space, absorbing boundary conditions must be applied.

2.5.1 Absorbing Boundary Conditions for FDM

The non-reflecting boundary conditions used in the finite difference formulation were developed by Cerjan et al. [41] and described as a sponge boundary. The method is based on a gradual reduction of the amplitude of the wave in a strip of nodes along the boundaries of the domain seen in Fig.8. The amplitudes on the strip of nodes are reduced via exponential decay.

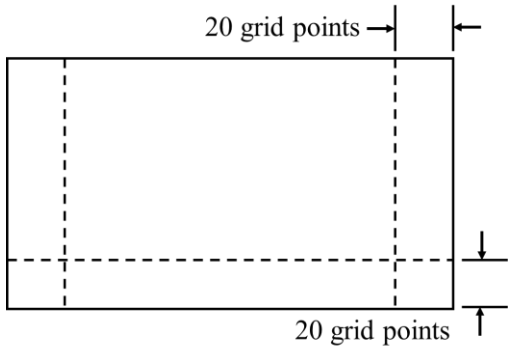

Figure 8. Grid configuration of the non-reflecting boundary conditions [41].

Another method that is frequently used for implementing non-reflecting boundary conditions is known as PML, which stands for a perfectly matched layer. The method was first used to simulate absorbing boundary conditions for electromagnetic waves [42] and has since been applied to elastic wave problems [43].

2.5.2 Absorbing Boundary Conditions for FEM

In COMSOL, absorbing boundary conditions can be applied for a set of elements along the boundaries of the domain with a desired layer thickness. The recommended thickness of the layer should be equal to the largest wavelength in the model. The absorbing boundary condition first applies a ‘scaling’ to the propagating wave so that once it reaches the defined boundaries, the wave will slow down. It then applies filtering to attenuate and filter out high-frequency components of the wave [40].

2.5.3 Free Surface Boundary Condition

To accurately model propagating waves on a surface, namely Rayleigh waves, a free surface must be incorporated into the model. On the free surface, the shear stress and vertical normal stress must be equal to zero. For the FEM, this is automatic for any undefined boundary in the domain, however, for finite difference, there are a few complications that make it more difficult to incorporate this boundary condition because when using the staggered grid, the shear stress is not available on the free surface.

A free surface was applied using an improved vacuum method by Zeng et al. [44], to generate Rayleigh waves on the surface. The original vacuum method suggested putting the material properties above the surface to 0, however, this did not fulfill the boundary condition [45]. Therefore, Zeng et al. improved this method by applying the parameter averaging scheme of Moczo et al. [5], which is that volume harmonic averaging is chosen for the shear modulus and volume arithmetic averaging for density. Combining this with the method presented by Mittet [45], which stated that the averaged shear modulus should be zero if any of the modulus values involved in the averaging are zero for the shear stress to be zero, the following scheme was derived:

$$\bar{b}_x = \begin{cases} 0, & if\ \rho_{i,k} = 0\ and\ \ \rho_{i+1,k} = 0 \\ \dfrac{2}{\rho_{i,k} + \rho_{i+1,k}} & otherwise; \end{cases} \tag{46}$$

$$\bar{b}_z = \begin{cases} 0, & if\ \rho_{i,k} = 0\ and\ \ \rho_{i,k+1} = 0 \\ \dfrac{2}{\rho_{i,k} + \rho_{i,k+1}} & otherwise; \end{cases} \tag{47}$$

$$\bar{\mu}_{xz} = \begin{cases} \left[\dfrac{1}{4}\left(\dfrac{1}{\mu_{i,k}} + \dfrac{1}{\mu_{i+1,k}} + \dfrac{1}{\mu_{i,k+1}} + \dfrac{1}{\mu_{i+1,k+1}}\right)\right]^{-1} & if\ \mu_{i,k}, \mu_{i+1,k}, \mu_{i,k+1}, \mu_{i+1,k+1} \neq 0 \\ 0 & otherwise \end{cases} \tag{48}$$

With this scheme, the shear stress on the surface will be zero because there will be a shift in the grid that is half the grid space distance. Therefore, only v_z and σ_{xz} are present on the surface.

2.6 Seismic Source to Incite Wave Propagation

In practical applications, the seismic source to incite wave propagation can be generated from nature, by hammering a plate on the ground on a plate, an explosion, or by dropping a mass. In numerical simulations, mostly in the case of seismic surveys, two types of sources including the Gaussian function and the second derivative of the Gaussian in time, called a Ricker function, can be used. The reason for choosing these two functions is that they are close to the signal of a hammer-hit pulse. The source used in this thesis was a Ricker wavelet, which is often used to model seismic events. The equation for a Ricker wavelet is:

$$R(t) = \left(1 - 2\pi^2 {f_M}^2 (t - t_0)^2\right) e^{-\pi^2 f_M (t - t_0)^2} \tag{49}$$

where f_M is the peak frequency of the source spectrum, t is time, and t_0 is the excitation time. A plot of the Ricker function is shown in Fig.9.

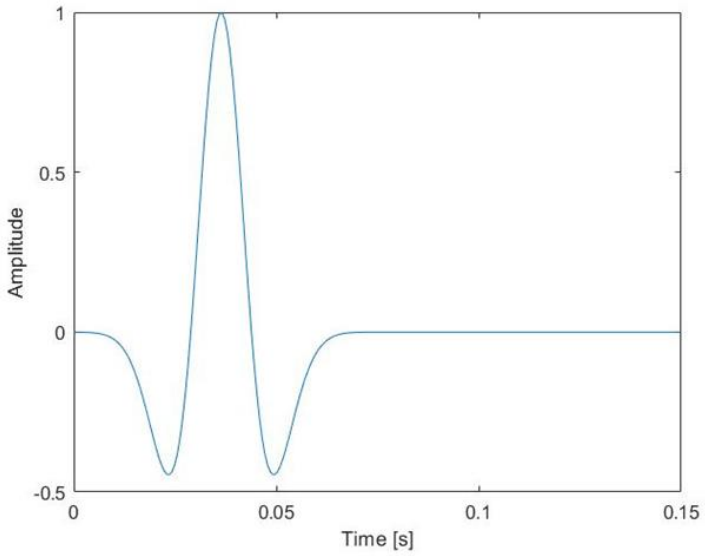

Figure 9. Ricker wavelet with a peak frequency of 30 Hz.

For the displacement formulation, the source was incorporated as a displacement. For stress-velocity, it was incorporated into the vertical velocity on a nodal point. The peak frequency employed depended on the material properties and the size of the domain of interest. For a larger domain (2000m × 2000m), 30 Hz is enough to excite the domain [46]. For a smaller domain, for

instance, a 50m × 20m domain, a larger frequency will need to be used to generate waves in the domain. For the FEM, the source was incorporated as a boundary load, where its location was dictated by a Gaussian function and then multiplied by the Ricker wavelet. The Gaussian function was depicted by,

$$G(x,y) = \frac{1}{\pi d} e^{-\left((x-x_0)^2 + \frac{(y-y_0)^2}{d}\right)} \tag{50}$$

where d is the source extent and x_0 and y_0 are the source's location in the domain.

2.7 Validation and Grid Study of Numerical Methods

2.7.1 Validation of 1-D Codes

The numerical and actual wave speeds were compared to validate the 1-D codes. This was completed by plotting the displacement at two different points in time and then picking the same points on each wave (in this study the apex of the wave was chosen) and then calculating the velocity. The actual velocity for this case was 316m/s, and the numerical velocity was also calculated to be 316m/s when calculating with this method with the waveforms in Fig.10. FDM and FEM produced identical figures.

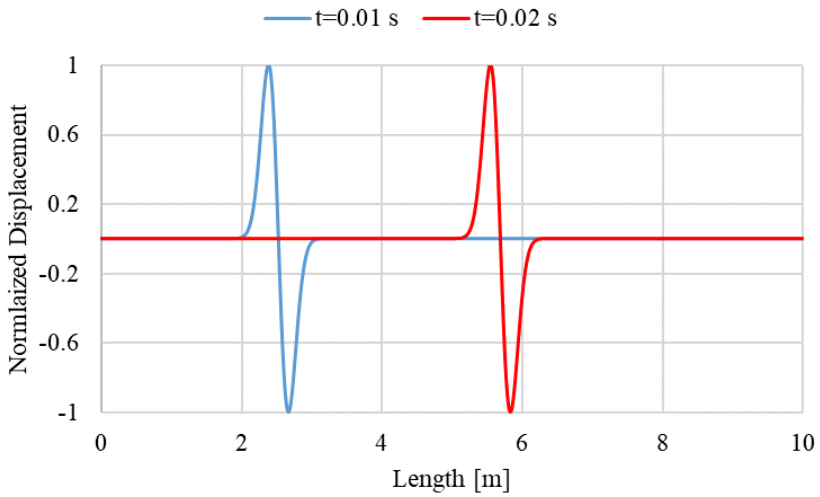

Figure 10. Normalized displacement at 0.01 s and 0.02 s.

2.7.2 Validation of Staggered Grid

The staggered grid FDM code created in MATLAB was validated by comparing it to the work of DeBasabe and Sen [46], which analyzed different finite difference algorithms with a fluid-solid interface. Their setup consisted of an upper fluid-half space and a lower solid-half space with the properties presented in Table 1. The source was a 30 Hz Ricker wavelet located 0.1km above the interface in the fluid domain. The step size they employed for the 2^{nd}-order staggered grid FDM was 2.5m for a 2km × 2km domain, and the boundaries were rigid.

Table 1. Material properties used in [45].

Domain	P-Wave Velocity [m/s]	S-Wave Velocity [m/s]	Density [kg/m^3]
Fluid	1500	0	1000
Solid	2700	1400	1200

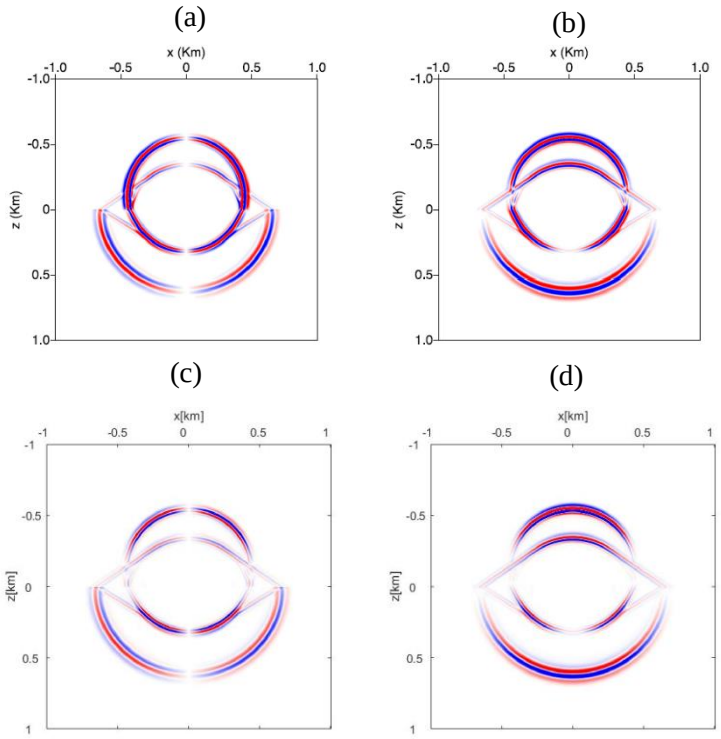

Figure 11. Comparison of [46] (a-b) with the current developed staggered-grid code (c-d). Horizontal particle velocity is (a) and (c) and vertical particle velocity is (b) and (d).

From Fig.11, the results of the developed staggered grid code closely match the wavefield data seen in [46].

In addition to comparing snapshots of the velocity fields, the travel time of the waves were computed by creating a shot gather on the surface of a homogeneous domain to additionally validate the code. A shot gather was created by saving the time history at various points in a line in the domain and then plotting them together to analyze how the wave travels. The wave speed can be calculated by calculating the slope of the P-wave and comparing it to the actual P-wave velocity. However, first, a grid study was completed for a homogeneous case to assure minimal dispersion.

2.7.3 Grid Convergence Study

The accuracy of the solution in numerical modeling strongly depends on conducting a systematic meshing exercise called the grid convergence study, which is usually performed to eliminate any possibility of the result relying on the size of the grid in the computational domain. In the grid study, a series of grid systems will be generated, and numerical computations will be performed to analyze the variation in results with each grid system.

The domain to be used for the rest of this thesis is one that is 50m × 20m. The grid study is completed using this domain by analyzing wave dispersion for three different spatial step sizes, which h were h=0.2m, 0.1m, and 0.05m. A uniform grid is considered for the computational domain and a 500Hz ricker wavelet was applied at the center on the free surface of the domain. The time histories of wave propagation are calculated at the first receiver 3m from the source and other receivers that are located 1m apart from each other. The properties of the homogeneous domain are the solid properties presented in Table 1. The results of the grid convergence study are presented in Fig.12. According to the numerical results which show the wave propagation for three different grid sizes, significant dispersion can be seen in Fig.12-a, which can be identified by the "tail" on the end of the Rayleigh wave. Dispersion can minimally be seen with a step size of 0.1m and even more so with a step size of 0.05m, but since the computational time doubles when the step is halved, the step size used for the source function and the material properties is 0.1m.

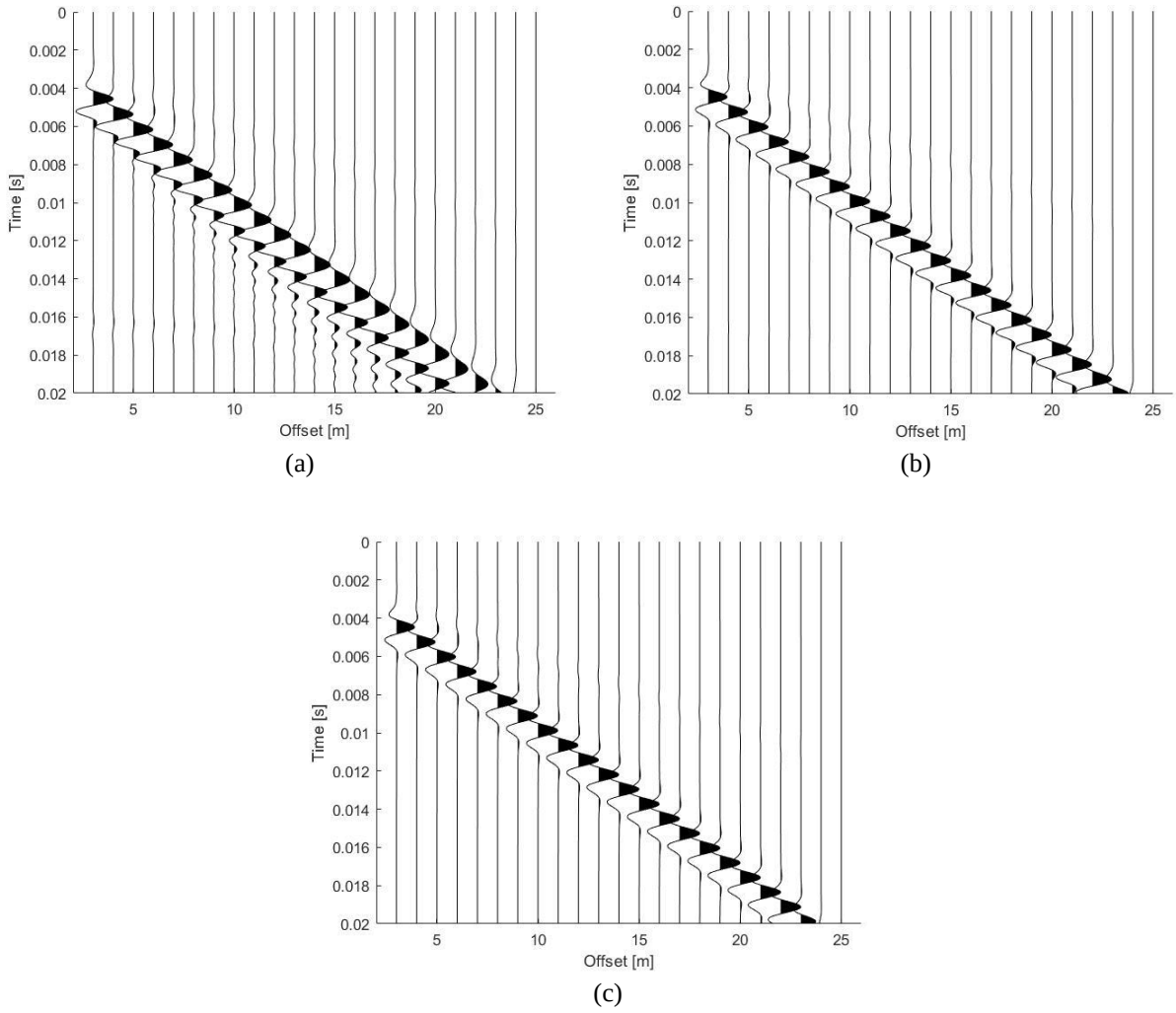

Figure 12. Comparison of vertical particle velocity for different grid sizes of (a) $\boldsymbol{h}$=0.2m, (b) 0.1m, (c) 0.05m.

The P-wave velocity can be calculated by the slope of the P-wave seen in vertical surface seismograms. Two spots were picked on the P-wave, and the resulting velocity was 2651.6 m/s for the FDM, which is close to the defined value of 2700 m/s. The slope is indicated with the red line in Fig.13. The error can be attributed to the picking of the points.

The grid size used for the FEM is recommended by COMSOL that the maximum element size can be:

$$\Delta x_{max} = v_r/(2 * f_o)/1.5 \tag{51}$$

where f_o is the peak source frequency and c_r is the Rayleigh wave speed approximated by:

$$v_r = v_s\left(\frac{0.87 + 1.12\nu}{1 + \nu}\right) \tag{52}$$

where ν is the Poisson's ratio.

The same method was used to calculate the P-wave velocity from the seismogram, where for FEM the numerical velocity was calculated to be 2640.2 m/s, where the error can also be attributed to the picking of the points. The result of wave propagation obtained by the FEM is presented in Fig.13, where the red line is the slope of the P-wave propagation. As shown in this figure, the results perfectly validate the software output and MATLAB's results in FDM.

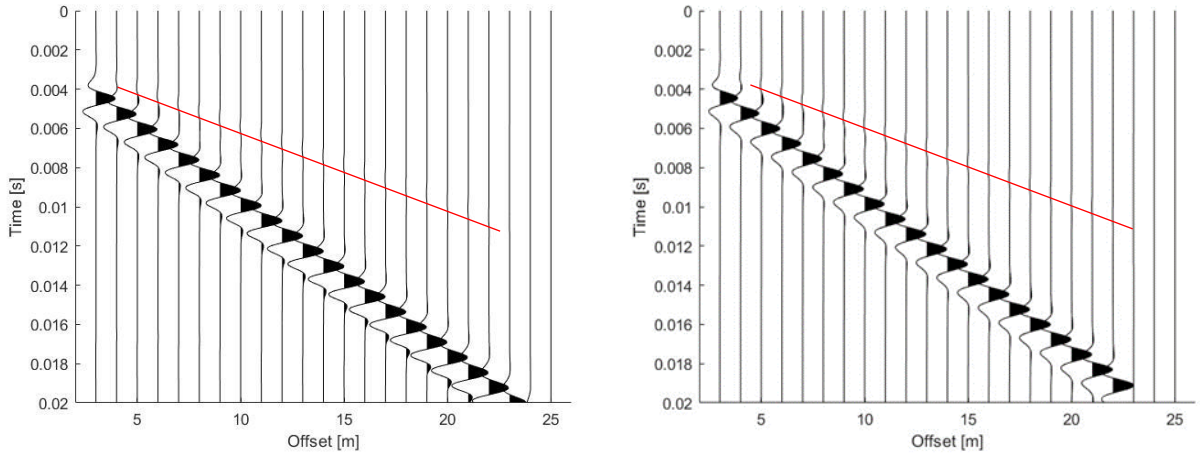

(a) (b)

Figure 13. The results of wave propagation using the FDM (a) and FEM (b).

2.8 Void Incorporation

The voids in the subsurface needed to be incorporated differently depending on the methodologies. Three void shapes including a 2m diameter circle, a 2m square, and a 2m (major axis) by 1m (minor axis) ellipse were studied (Fig.14). For the FDM, the shape is defined on the grid using the circle/ellipse equation, and the material properties of the void are all set to 0 to represent a vacuum. This resulted in a staircase approximation for the circle and ellipse case because they are defined on a structured grid that is created using the FDM, seen in Fig.15. Because

it is a staircase approximation, the results may contain some errors at the boundaries of the defined shape. To combat this, a different grid type would have to be employed to account for circular-shaped voids. Voids are incorporated in COMSOL by defining the shape of the void in the computational domain. Various meshing operations can be applied to correctly define circular shapes. In the grid system, mesh size varies throughout the domain, where finer mesh sizes are applied near the void to accurately capture the reflections from the void.

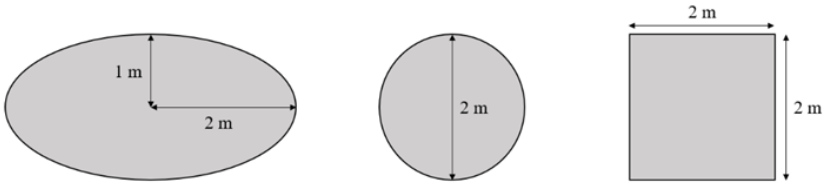

Figure 14. Void shapes incorporated into the domain.

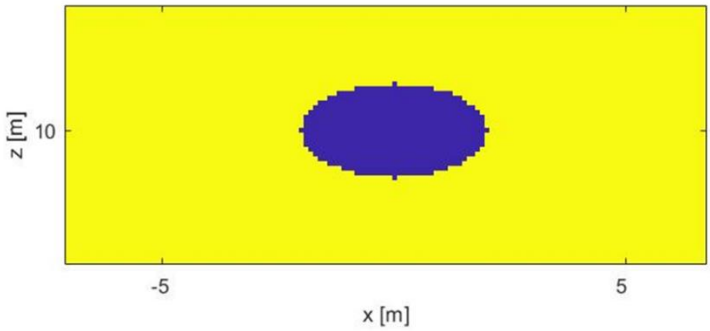

Figure 15. Stair-case approximation for an elliptical void in a homogenous domain.

Chapter 3: Analysis of Wave Propagation with No Voids

3.1 1-D Modeling Results

The 1-D modeling of the elastic wave equation was completed using the FDM and FEM. The setup featured a bar with its free end subjected to axial impulse traction, $R(t)$, which was a Ricker wavelet, and the other end was fixed, as seen in Fig.16.

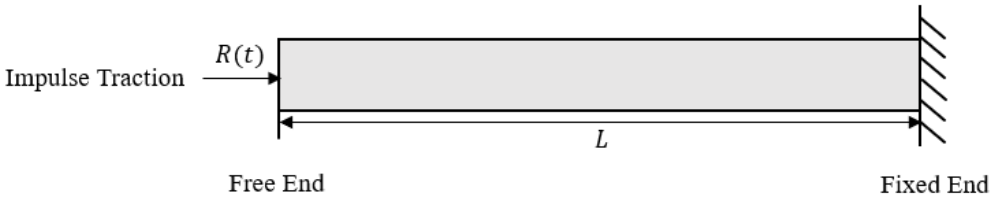

Figure 16. Schematic diagram of 1-D setup.

3.1.1 Single-Layer Case Study

A homogeneous case was first analyzed with the material properties in Table 2, which are fictitious values used to study their effect. The spatial step size for each simulation was 0.01m and the time-step for each method was depicted by Eq. (7). All results were normalized by dividing the resulting waveform by the maximum value of displacement.

Table 2. Material properties for 1-D setup.

Property	Value
Young's Modulus ($\boldsymbol{E}$)	100 MPa
Density ($\boldsymbol{\rho}$)	1000 kg/m^3

The source was a Ricker wavelet with a central loading frequency of 500Hz and was analyzed for a Courant value of 1. This resulted in a singular wave that traveled through the domain at a velocity of 316m/s. As time moved, the amplitude of the wave was preserved, and dispersion did not occur. The waveform is presented in Fig.17.

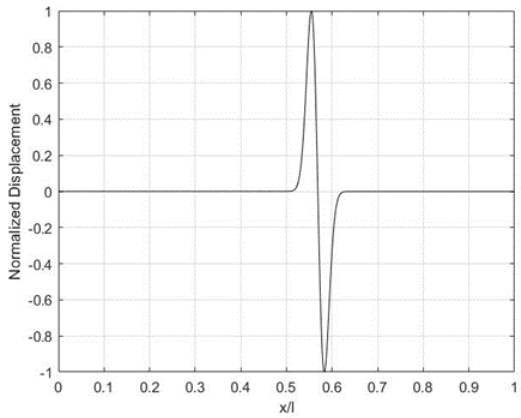

Figure 17. FDM: Normalized displacement at 0.02s for $\boldsymbol{C}$=1 and $\boldsymbol{f}$=500Hz.

The FEM results were identical to Fig.17. To analyze the manifestation of dispersion, the Courant number is set to 0.5. When dispersion starts, the amplitudes of the upper and lower portion of the wave first begin to vary, where at a certain point, the lower frequency component of the wave begins to trail behind the main wave, as seen in Fig.18.

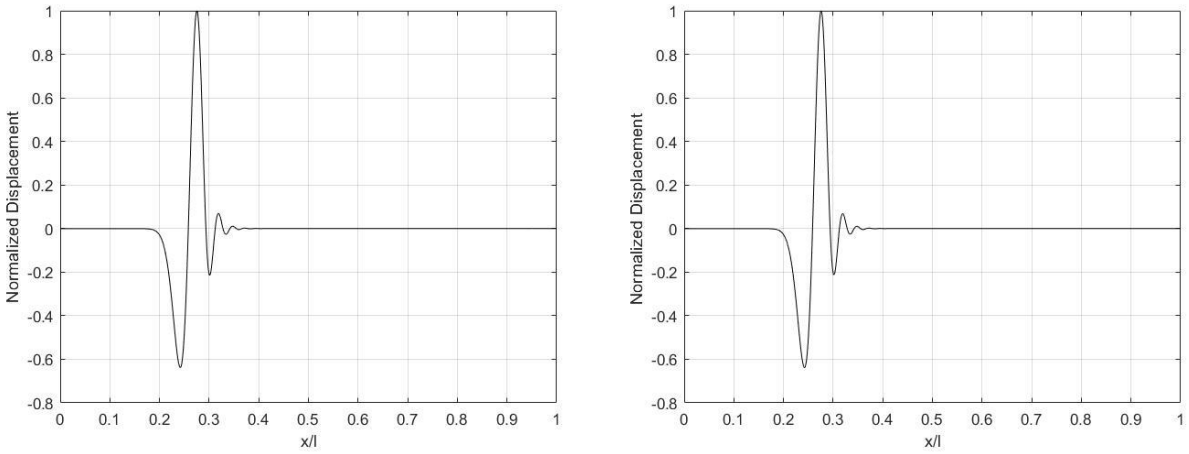

(a) (b)

Figure 18. FDM (a) and FEM (b) displacement plots at 0.5 s for $\boldsymbol{C}$=0.5 and $\boldsymbol{f}$=500 Hz.

FDM and FEM produce identical results for the onset of dispersion. For the second case, a 1200Hz source was analyzed C=0.5. The dispersion is much more pronounced in Fig.19 when compared to Fig.18 with a 500Hz source frequency. Additionally, the original wave form is no longer recognizable. To lessen the effect of dispersion, the spatial step needs to be increased, however, dispersion will still occur due to the Courant number.

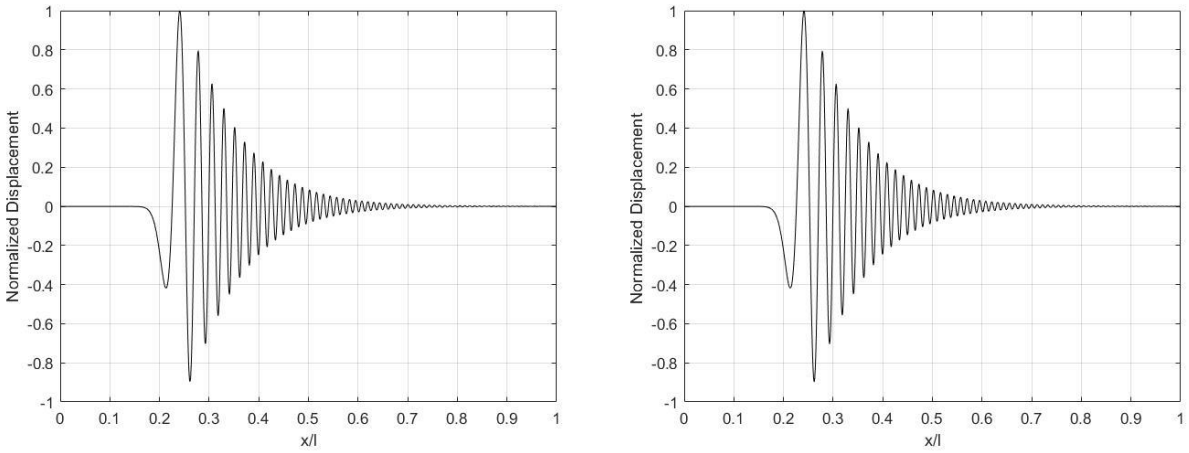

(a) (b)

Figure 19. FDM (a) and FEM (b) displacement results at 0.5s for $\boldsymbol{C}$=0.5 and $\boldsymbol{f}$=1200 Hz.

3.1.2 Two-Layer Case Study

The model under investigation was a bar comprised of two materials with differing densities, where the second material was placed at $x/l = 0.5$. The time stepping depended on the smallest density in the bar to prevent instability. The density in the left half of the bar was 1000 kg/m^3 and the right half was 2000 kg/m^3. For $C = 1$, the left side exhibited this value whereas the right side was $C = 0.707$. A portion of the wave reflects at the interface and the remaining was transmitted to the other medium, as seen in Fig.20. At the point of time shown in Fig.20, dispersion was not prominent, where there was only a slight change in the upper and lower portion of the wave in the right half of the domain. For the 1200Hz case, dispersion occurred at a quicker rate, as seen in Fig.21.

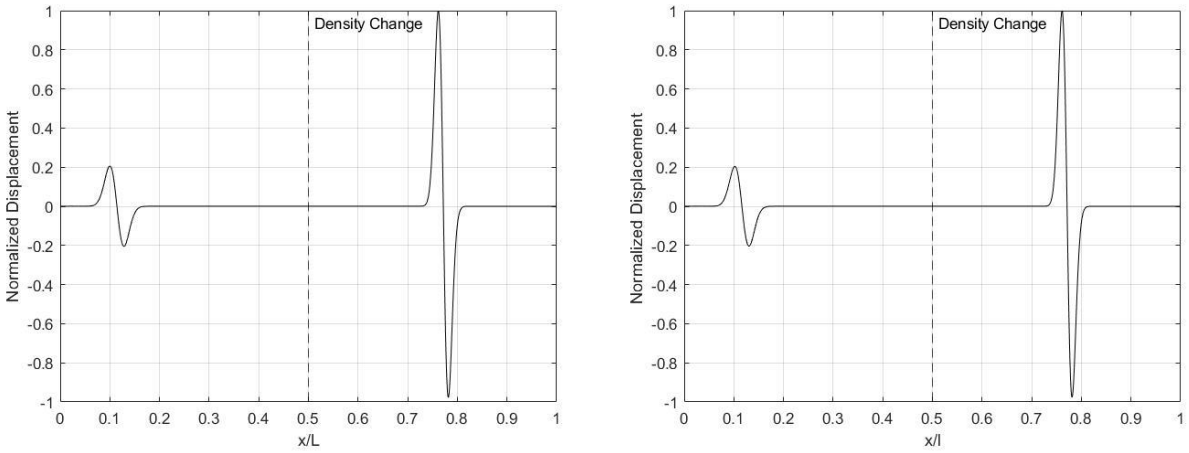

(a) (b)

Figure 20. Displacement plots for two materials at 0.03 s and f=500 Hz for FDM (a) and FEM (b).

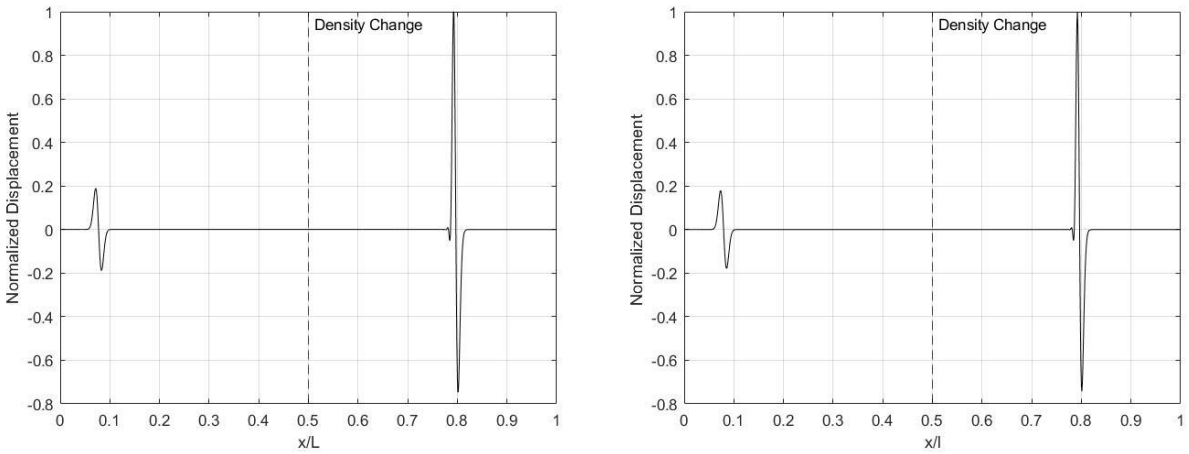

(a) (b)

Figure 21. Displacement plots for two materials at 0.03s and f=1200Hz for FDM (a) and FEM (b).

3.1.3 Computational Cost and Implementation

The FDM was simpler to implement than the FEM and both methods produced identical wave propagation results. Computationally, the FEM code had slightly longer simulation times compared to FDM. Either method can efficiently be utilized to analyze 1-D wave propagation with and without layers.

3.2 2-D Analysis of Wave Propagation with No Voids

Four models were created that analyzed the wave propagation with no voids. A homogenous rock domain, a homogenous soil domain, a four-layered domain, where the material properties were determined by ultrasonic testing, and a three-layered domain with a harsh difference in material properties were studied. For these analyses, the staggered grid scheme was used for the FDM. For the FEM, COMSOL was used for the simulation of 2-D wave propagation. The displacement finite difference formation was analyzed by using the setup used in Section 2.7.2 which had fluid upper half-space and lower solid half-space. The results are presented in Fig. 22, which displayed that the displacement-non-staggered grid scheme is unable to model a case with fluid and the solution heavily diverges in the fluid domain. Due to this, it cannot model a vacuum because the material properties need to be set to 0 to model it. For the remaining part of this thesis, the staggered grid was used for modeling elastic waves with the FDM for both cases of with and without a void.

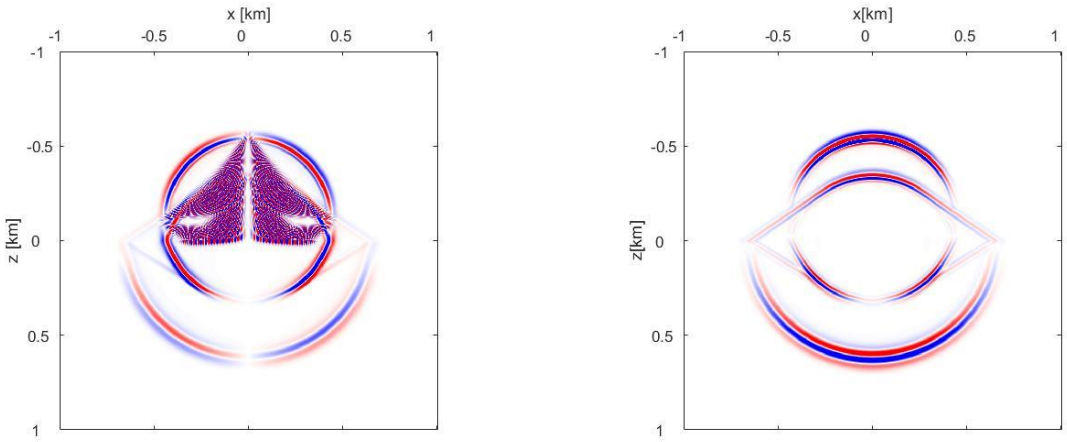

(a) (b)

Figure 22. Vertical displacement using displacement FDM (a) and vertical particle velocity using staggered grid FDM (b) at 0.04s.

3.2.1 2-D Wave Propagation in Rock and Soil

2-D wave propagation in a single-layer domain including soil and rock is presented separately in this section. The properties used for each material are shown in Table 3.

Table 3. Material properties used in homogenous domain trials.

Domain	P-Wave Velocity [m/s]	S-Wave Velocity [m/s]	Density [kg/m^3]
Rock	1449.4	1057.9	2608.7
Soil	320	130	1700

The rock properties were determined using ultrasonic testing. The size of the domain was 50m×20m and the source was a 300Hz (rock) and 50Hz (soil) ricker wavelet located on the center of the surface. Due to the smaller velocity values that make up a soil, a lower source frequency was used when analyzing this domain to keep computational cost low. Receivers were placed 3m right of the source and located 1m apart.

Figure 23 displays the FDM results of wave propagation through a series of snapshots, showing the vertical particle velocity in the rock domain. Each wave type can be seen in the snapshots, which are the P-wave, S-wave, and Rayleigh wave. The snapshots of the FEM results using COMSOL are shown in Fig.24 which also displayed the proper waveforms expected for elastic wave propagation. Both FDM and FEM results produced similar snapshots. The time history recorded by the receivers is compared for each method in Fig.25.

(a)

(b)

(c)

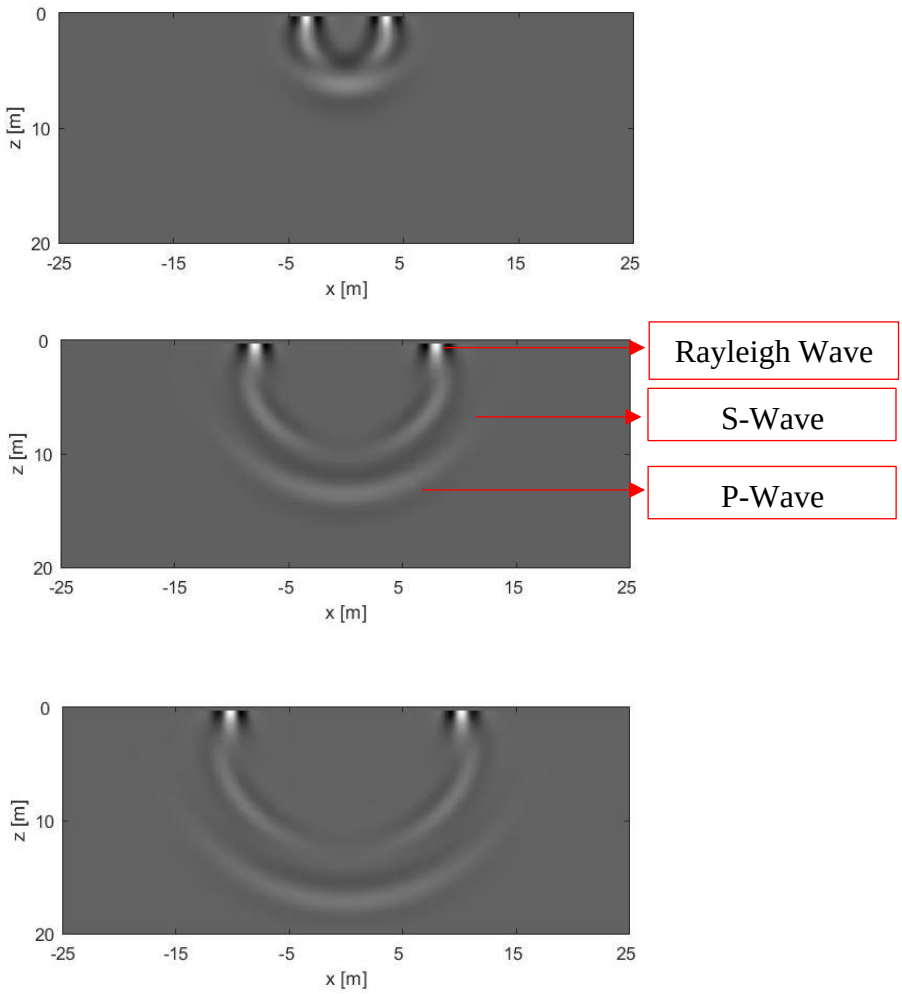

Figure 23. Vertical particle velocity in a rock domain at 0.0075s (a), 0.0125s (b), and 0.015s (c) using FDM.

(a)

(b)

(c)

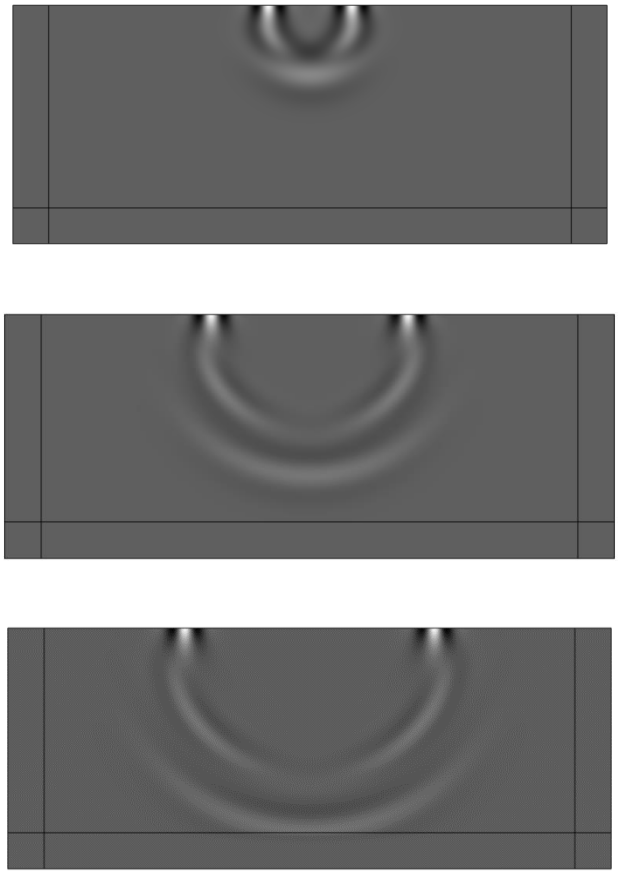

Figure 24. Vertical particle velocity in a rock domain at 0.0075s (a), 0.0125s (b), and 0.015s (c) using FEM.

As seen in Fig.25, there are minimal differences between the time histories generated with each method. There is insignificant dispersion in the FDM results, which can be identified on the tail end of the main wavefront. This dispersion is not seen in the FEM results. Fig.26 shows the time histories of vertical particle velocity on the surface for the soil domain using each method.

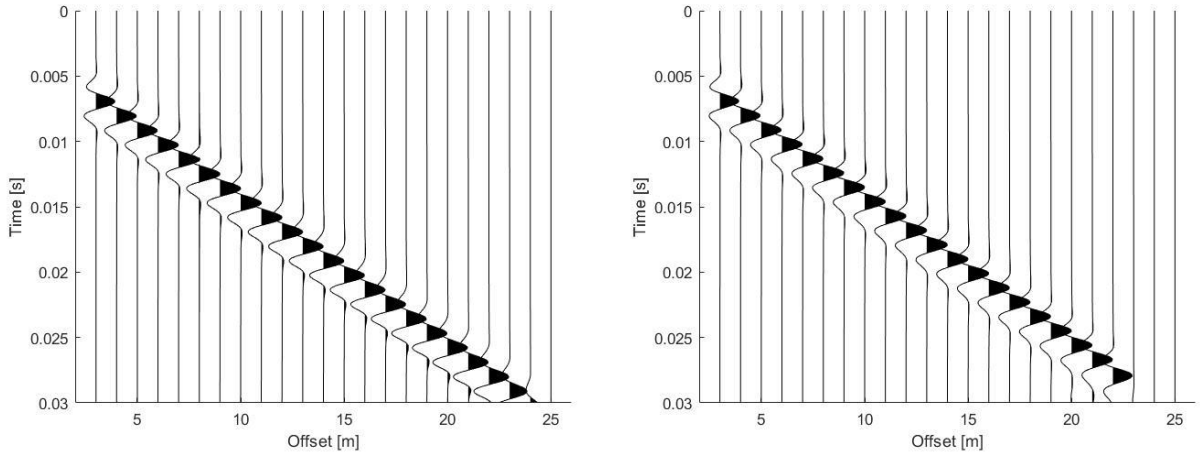

(a) (b)

Figure 25. Time history of vertical particle velocity on the surface using FDM (a) and FEM (b) for a rock domain.

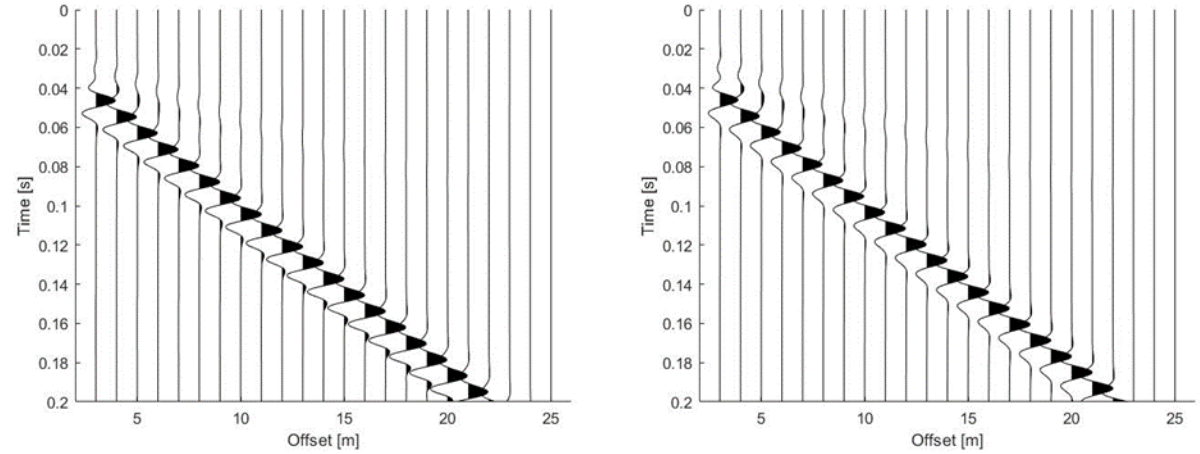

(a) (b)

Figure 26. Time history of vertical particle velocity on the surface using FDM (a) and FEM (b) for a soil domain.

The time histories generated for a soil domain are also similar between each method. Because of the properties used, the wave needed more time to propagate through the domain, which is to be expected.

3.2.2 2-D Wave Propagation in a Four-Layer Domain from Ultrasonic Testing

A four-layered domain was analyzed with both the FDM and FEM method. To create a more realistic model, ultrasonic testing was completed on samples from a borehole collected at a local site. The measurements were taken with the Proceq© Pundit Plus device with their 54kHz P-wave transducers and 40kHz Dry-Point shear wave transducers. The obtained results are presented in Table 4.

Table 4. Velocity results obtained with ultrasonic testing.

Sample	Depth [m]	P-Wave Velocity [m/s]	Standard Deviation	S-Wave Velocity [m/s]	Standard Deviation	Density [kg/m^3]
1	0m to 5m	1449.4	13.41	1057.9	6.74	2608.7
2	5m to 8m	2041.7	20.53	1510.6	7.95	2202.5
3	8m to 12m	2322.0	16.86	1650.3	16.72	2566.5
4	12m to 20m	2550.7	29.35	1991.4	10.84	2443.5

Based on the results obtained from the ultrasonic tests with samples from different depths, a four-layered domain was generated for the numerical simulation (see Fig.27).

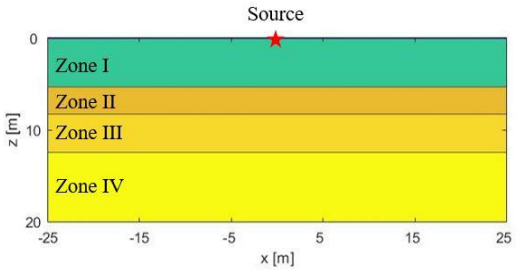

Figure 27. A four-layered domain from results of ultrasonic tests.

The source used to incite wave propagation was a 300Hz Ricker wavelet on the center of the surface. The receivers were 1m apart and started 3m right of the source impulse. The time history from each method is reported in Fig.28.

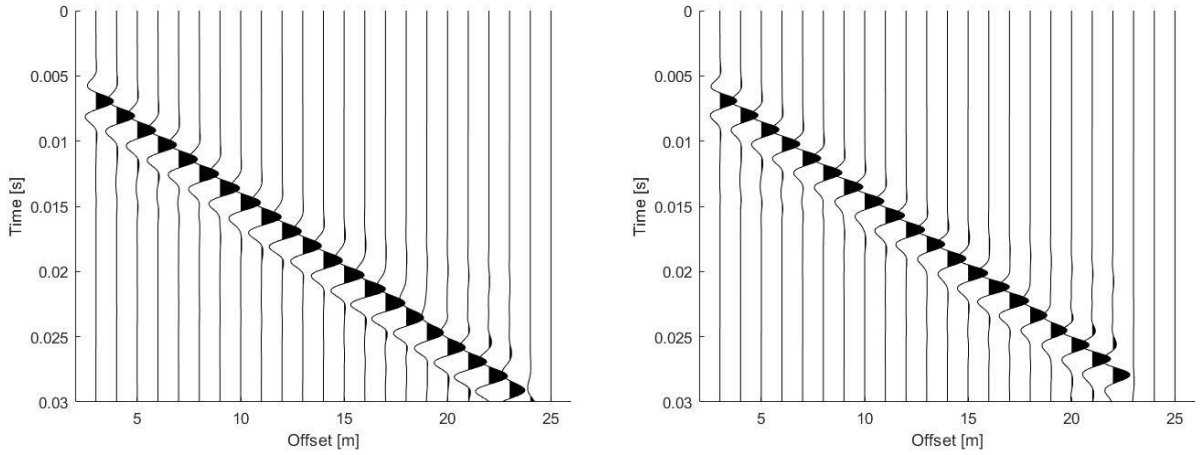

(a) (b)

Figure 28. Time history of vertical particle velocity of four-layered domain using FDM (a) and FEM (b).

There are reflections seen in Fig.28 that indicate that it is a layered domain, however, the reflections are difficult to see because the material properties are very alike.

Different source frequencies were analyzed with this model using the FDM to analyze how it effects wave propagation. The source frequencies applied to the four-layered domain were 100Hz, 200Hz, 300Hz, and 400Hz. With decreasing source frequency, the impulse source becomes wider, which results in what is seen in Fig.29. At 100Hz, it is difficult to distinguish the layers in the domain due to the size of the source function. At the other frequencies, reflections are slightly visible but still difficult to see.

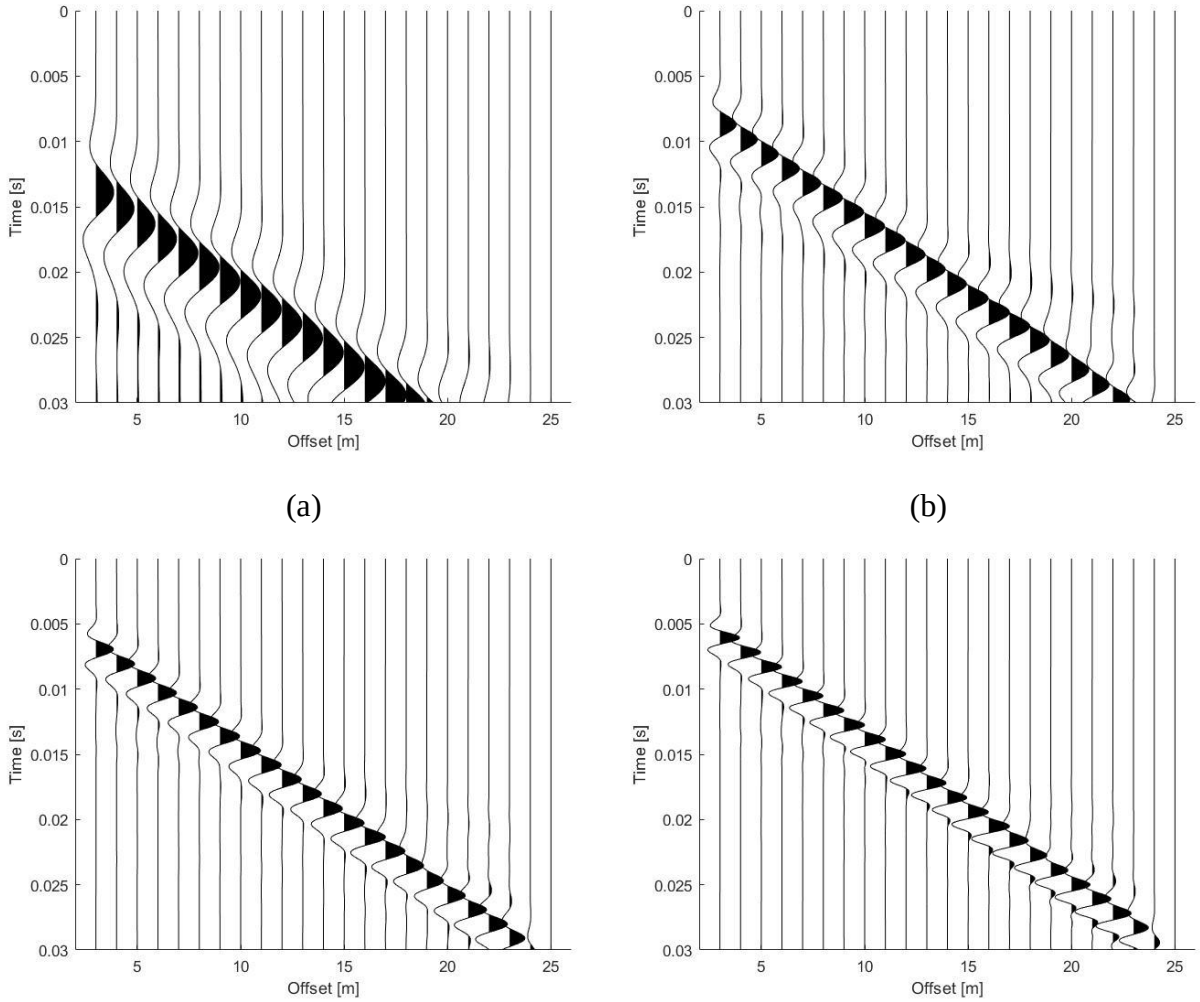

Figure 29. Time history of vertical particle velocity of a four-layered domain using FDM for 100 Hz (a) 200 Hz(b), 300 Hz (c), 400 Hz (d).

3.2.3 2-D Wave Propagation in a Three-Layered Domain

In a multi-layered domain, it is important to study wave propagation through interfaces with a significant jump in layer properties. Therefore, for such a study, a three-layered domain was generated based on the size and properties given in Table 5. The material in layer 1 was modeled as silty clay. Layer 2 was a clayey shale, and layer 3 was siltstone. Due to the small P- and S-Wave velocities in the top layer, a smaller source frequency (100Hz) was applied on the surface. Figure

30 displays the vertical particle velocity for both FDM and FEM. The range in Fig.30 was intentionally lessened to see the wave more clearly.

Table 5. Material properties for a three-layer domain.

Layer	Depth [m]	Density [kg/m^3]	P-Wave Velocity [m/s]	S-Wave Velocity [m/s]
1	0m to 6.67m	1798	720	280
2	6.67m to 13.33m	2660	2430	1430
3	13.33m to 20m	2240	3730	2140

As seen in Fig.30, the majority of the wave remained in the upper third of the domain. This is because of the vast difference in material properties between the first and second layers. The time history was recorded at the same positions as the previous cases and is presented in Fig.31. Various reflections can be seen from the seismogram and both methods generated comparable results.

(a)

(b)

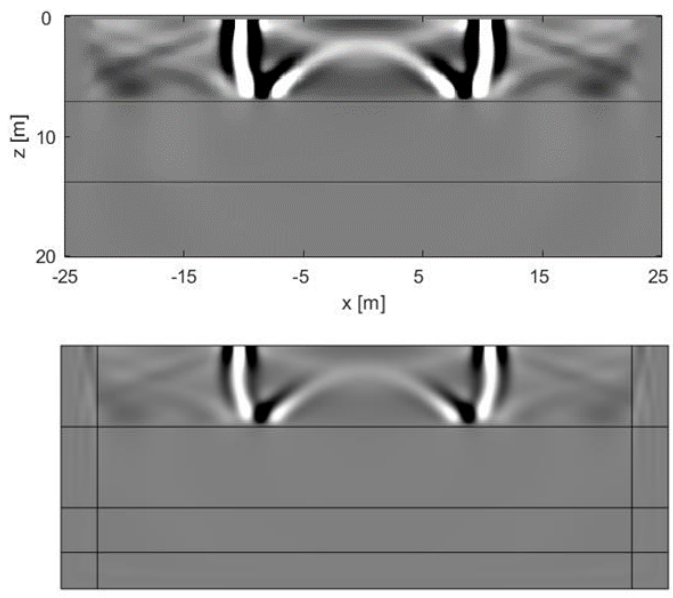

Figure 30. Snapshot of vertical particle velocity at 0.05s in a three-layered domain using FDM (a) and FEM (b).

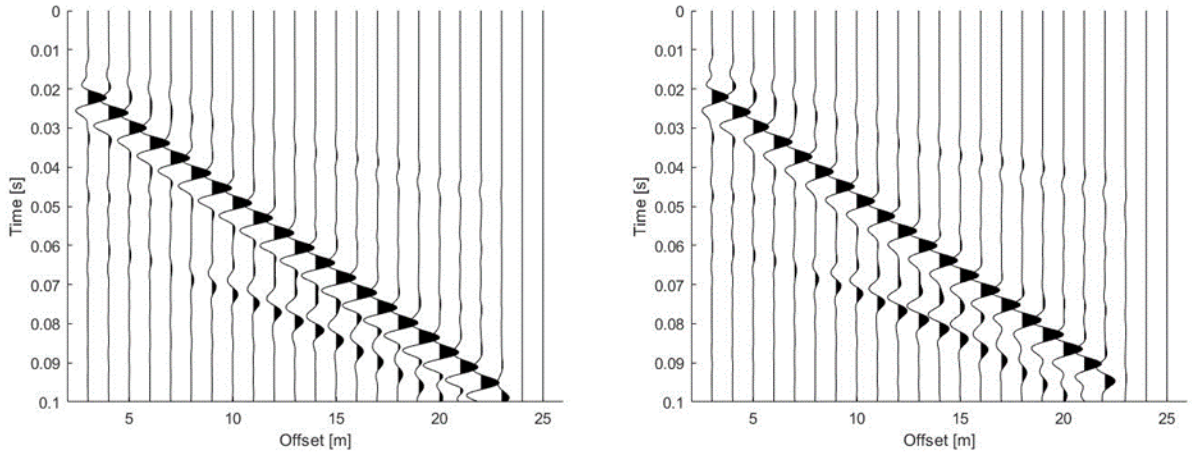

Figure 31. Time history of vertical particle velocity in a three-layered domain using FDM (a) and FEM (b).

3.3 Computational Cost and Implementation

Both methods produce comparable results for the homogenous and layered cases. All of the numerical methods were run on an Intel(R) Core i7-10700 CPU with 16.0 GB of RAM. To analyze computational times, each domain was run for a simulation time of 0.1s for 5 trials and then averaged. Computationally, the FDM had better run times than the FEM when comparing Table 6 and 7. The timestep chosen for both methods to produce stable results depended on the spatial step size and the maximum P-wave velocity in the medium. For the FDM, this was dictated by Eq. (42), which indicated that the largest P-wave velocity in the medium will determine the time step. Therefore, domains with larger P-wave velocities will require a smaller timestep if the spatial step is kept constant. Similarly, the timestep taken in COMSOL depends on the ratio of the spatial step and maximum velocity, [40]. In descending order, the domains with the largest P-wave velocity were the three-layered domain, four-layered domain, rock, and soil. Therefore, it is expected that the three-layered domain will have the longest simulation times because they exhibit the smallest time step, which is shown in Table 6 and 7.

Table 6. Computational times for the FDM.

Domain	Time Step [s]	Average FDM Time [s]	Standard Deviation [s]
Soil	2.210e-04	5.4	0.3
Rock	4.879e-05	26.8	1.0
Four-Layered	2.772e-05	36.9	1.3
Three-Layered	1.896e-05	57.2	0.4

Table 7. Computational times for the FEM.

Domain	Time Step [s]	Average FEM Time [s]	Standard Deviation [s]
Soil	1.085e-04	48.6	1.3
Rock	4.980e-05	66.0	0.7
Four-Layered	2.830e-05	130.4	1.5
Three-Layered	9.675e-06	503.2	1.8

The staggered-grid FDM was also simpler to implement into MATLAB, whereas it would be difficult to code the FEM in 2-D. Because of this reason, COMSOL was used, but it is a software that requires a license to use, which makes the FDM more appealing than the FEM. Both methods produced satisfactory results and there was no significant difference in the results of each method.

Horizontal layers were built in easily by changing the material properties in the given domains. However, if one wanted to model non-horizontal layers, the FEM would have the advantage because with the given FDM code, non-horizontal layers will have to have a staircase approximation. Computationally, the FDM had shorter runtimes compared to the FEM. Either method can be applied when analyzing elastic waves with horizontal layers.

Chapter 4: 2-D Analysis of Wave Propagation In Presence of a Void

The cases previously analyzed without a void in Chapter 3 are now studied with a void placed in the center of the domain. An elliptical void, circular void, and square void are examined in the rock domain, soil domain, three-layered domain, and the domain created from ultrasonic testing. When the void is placed in the homogenous domain, it is simple to predict when the reflections from the void can be seen on the surface seismogram by knowing the P-wave velocity and depth of the void. To reach the top of the void, which is located 9m from the surface, the time it will take the P-wave to reach the void is 0.0062s, which is then added to the excitation time of the source, where for 300Hz this was 0.0036s, which resulted in a total time of 0.0098s. This was calculated by Eq. (53).

$$t = \frac{x}{v_p} \tag{53}$$

where x is the depth of the void and v_p is the P-wave velocity. This time is then added to the time it will take the P-wave reflection to reach a receiver on the surface. For instance, if analyzing a receiver 5m from the source, the time it will take to reach the receiver will be 0.0071s (see Fig.32 for a visual representation of this method). The predicted time to see the reflection from the void is then calculated by adding the time it takes to reach the surface of the void to the time it took to reach the receiver. For a void whose surface is 9m from the surface and with a P-wave velocity of 1449.4m/s, this time was 0.0170s. For soil properties, this time was 0.0821s. These values are compared to when the P-wave reflection is seen on the seismogram produced by each method. This was not applied to the layered domain because it is more difficult to predict when and if the reflection can be seen on the seismogram since the waves interact with the layers and void.

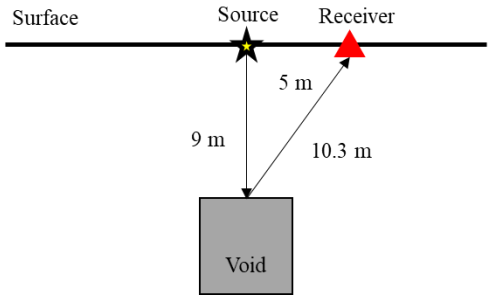

Figure 32. Schematic diagram used to analyze predicted void reflection on time history.

4.1 2-D Wave Propagation in Rock with a Void

The properties of rock are the same as used in the previous section, which is in Table 3. A snapshot of the wave propagation for both methods are presented in Figs.33-35 for an elliptical void, circular void, and square-shaped void, respectively. According to the numerical results, it can be observed that for an elliptical and circular void, there was minimal noise near the interface of the void using the FDM due to the staircase approximation. In all the snapshots, reflections can be seen due to the void's presence. Both methods produced similar wavefields.

(a)

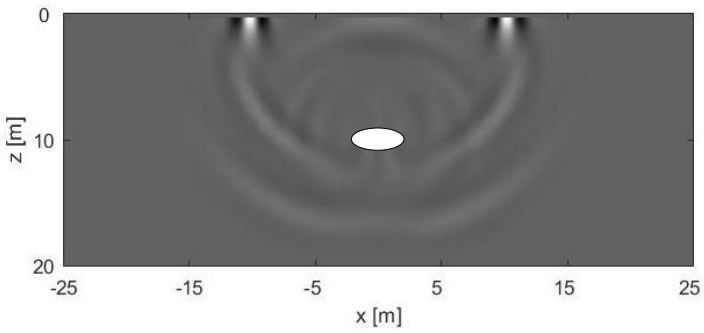

(b)

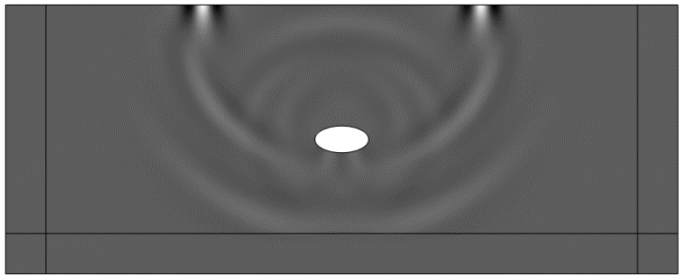

Figure 33. Vertical particle velocity at 0.015s with an elliptical void placed at the center of the domain using FDM (a) and FEM (b) in rock.

(a)

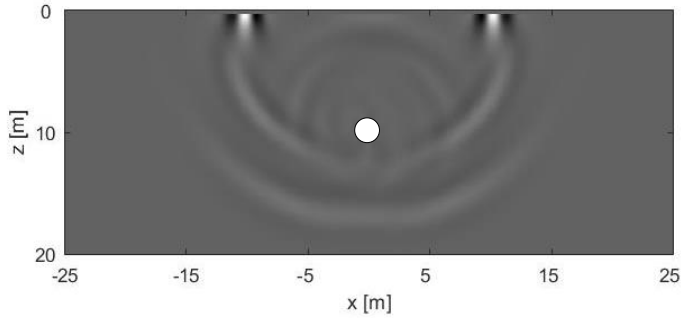

(b)

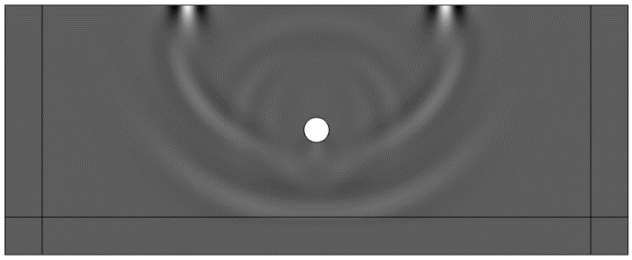

Figure 34. Vertical particle velocity at 0.015s with a circle-shaped void placed at the center of the domain using FDM (a) and FEM (b) in rock.

(a)

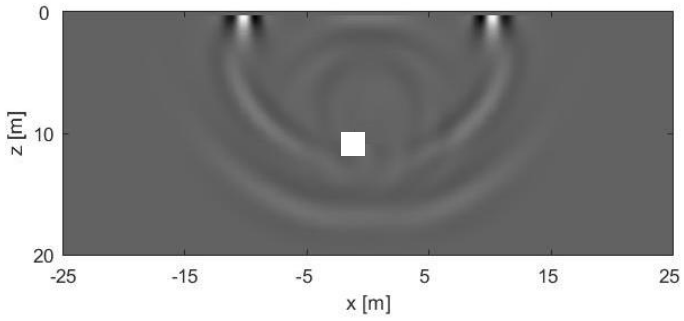

(b)

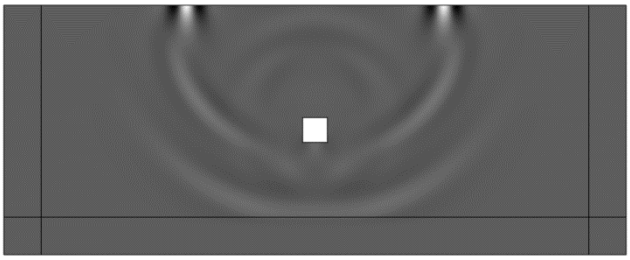

Figure 35. Vertical particle velocity at 0.015s with a square-shaped void placed at the center of the domain using FDM (a) and FEM (b) in rock.

The time history of vertical particle velocity was recorded on the surface for each void case. Figs.36-38 show the time history with an elliptical void, circular void, and square-shaped void, respectively. Visually, the first reflections can be seen at 0.015s-0.02s between 3m-9m in both methods. This time is in good agreement with the calculated value of 0.017s.

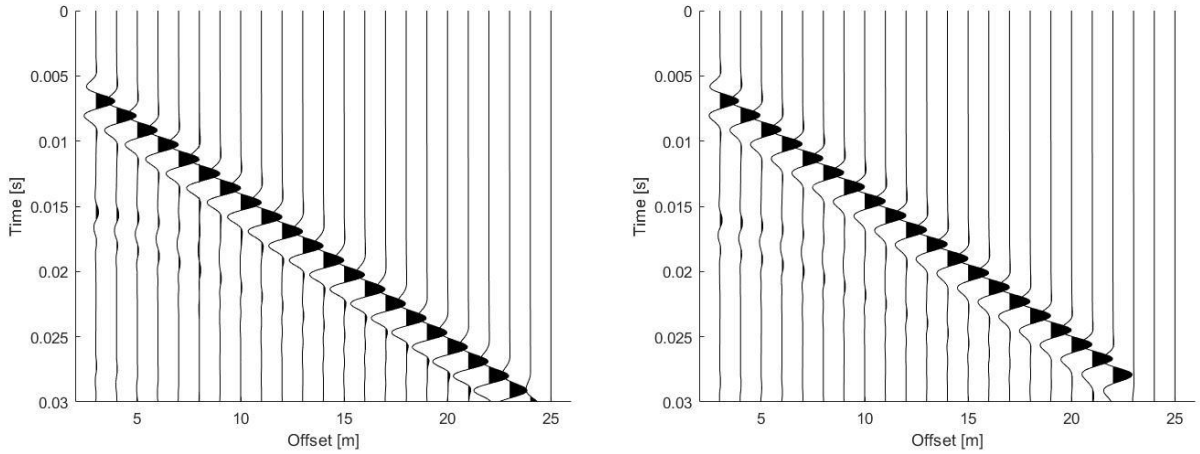

(a) (b)

Figure 36. Surface time history of vertical particle velocity with elliptical void using FDM (a) and FEM (b) in rock.

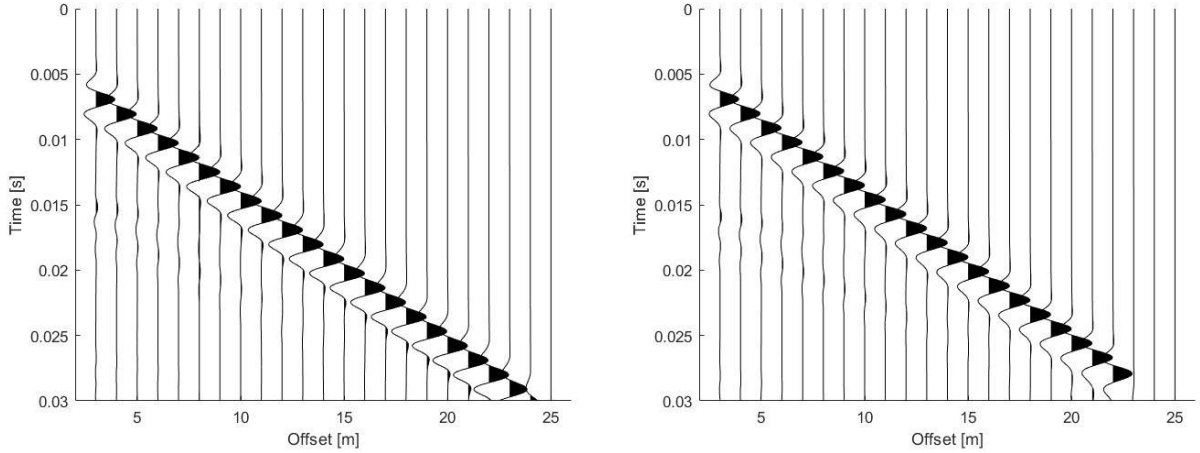

(a) (b)

Figure 37. Surface time history of vertical particle velocity with circular void using FDM (a) and FEM (b) in rock.

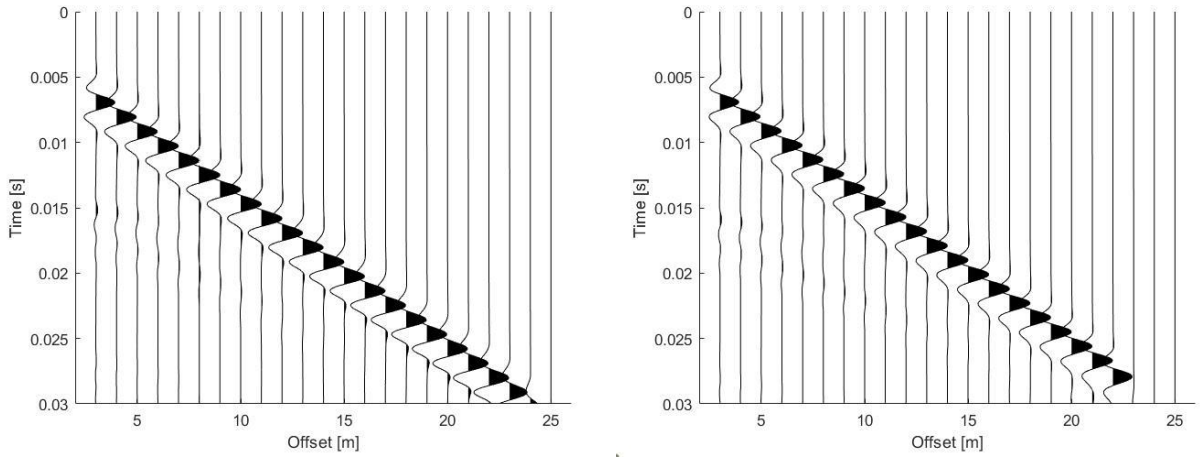

Figure 38. Surface time history of vertical particle velocity with a square-shaped void using FDM (a) and FEM (b) in rock.

Based on the results from Figs.36-38, the results mainly show the propagation of the surface wave, and it is hard to find the location of the void from the reflected P-waves. Therefore, to further investigate the effect of voids on wave propagation, these results were subtracted from the non-void results. The generated differences for the FDM are presented in Fig.39 and for the FEM in Fig.40.

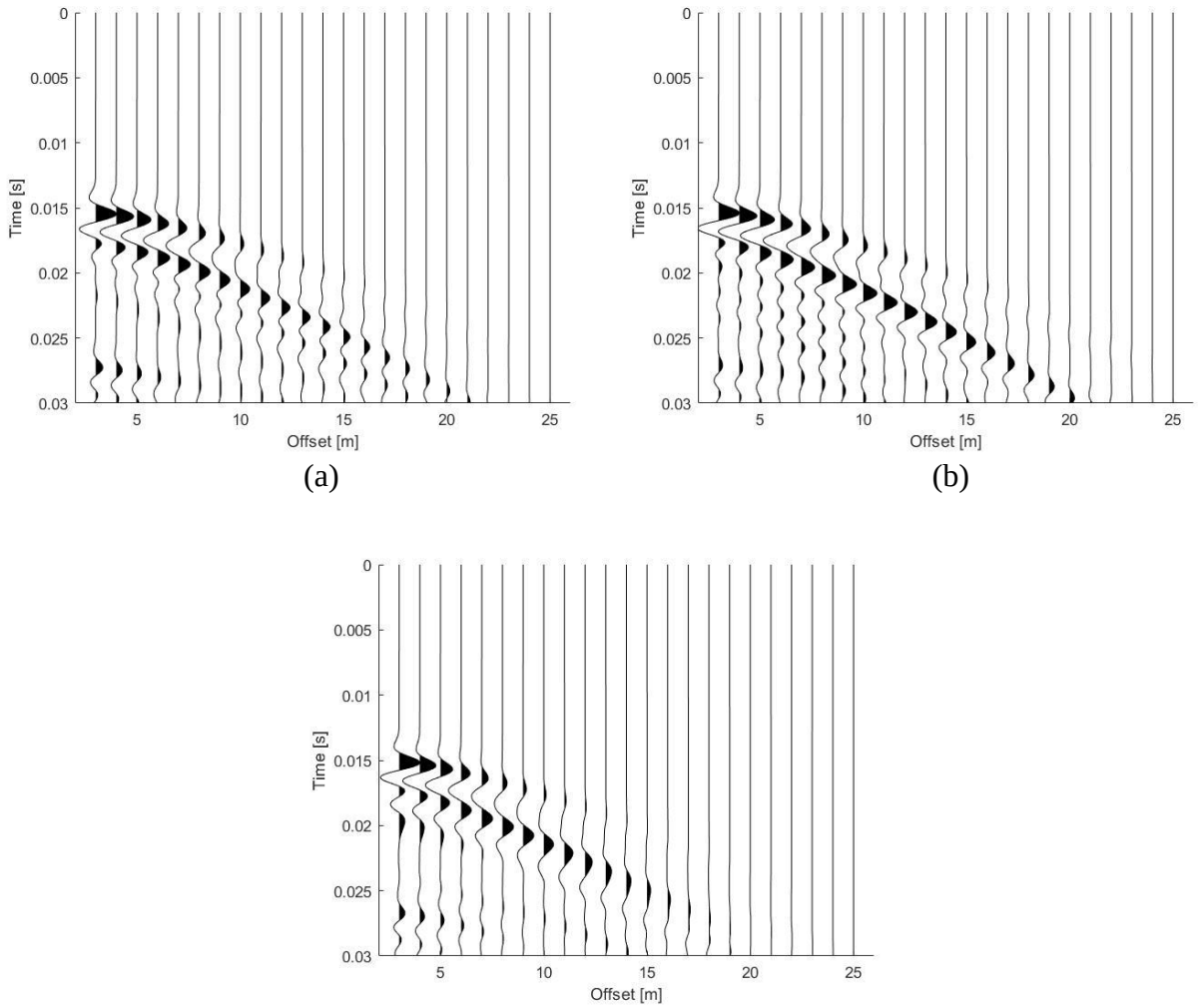

Figure 39. The subtracted vertical particle velocity in the case of void from the case without void for an elliptical (a), circular (b), and square (c) void in rock using FDM.

From Fig.39, the subtracted data generated by the P-wave reflection can be seen between 0.0015s and 0.02s and diminishes farther away on the surface. The maximum difference occurred at the first receiver at 3m for each case and had a value of 0.0028m/s, 0.0020m/s, and 0.0017m/s for the elliptical void, square void, and circular void, respectively. This indicated that the elliptical void had a more significant effect on wave propagation than the other void types. This is because the void is wider than the other analyzed shapes.

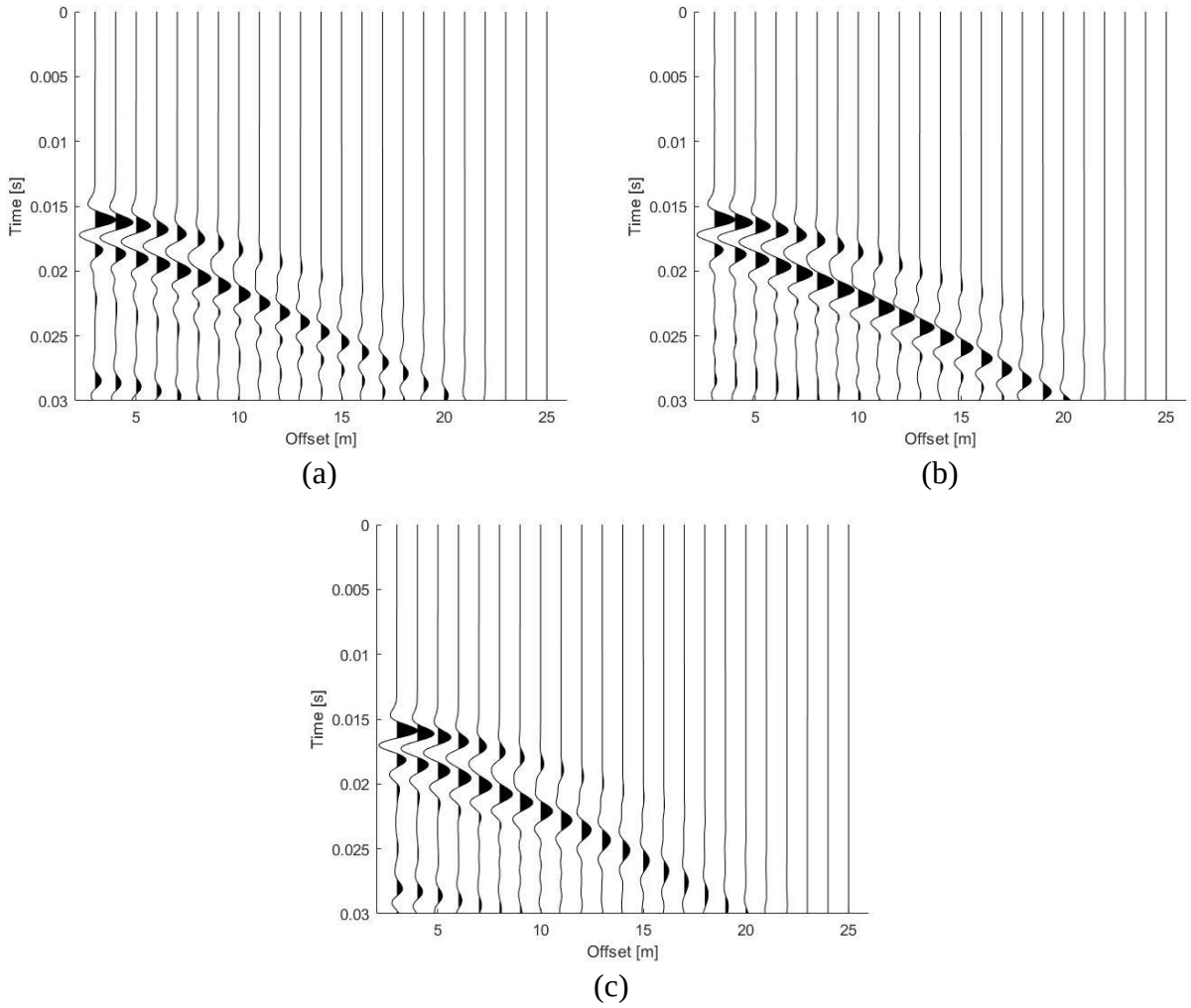

Figure 40. The subtracted vertical particle velocity in the case of the void from the case without void for an elliptical (a), circular (b), and square (c) void in rock using FEM.

For the FEM in Fig.40, the largest difference was seen also at 3m. The maximum difference at this point was 0.0021m/s, 0.0015m/s, and 0.0011m/s for the elliptical void, square void, and circular void, respectively. Similar to the FDM results, the elliptical void generated the largest difference while the circular void generated the smallest one.

4.2 2-D Wave Propagation in Soil with a Void

The same study in Section 4.1 was completed with a soil domain with the properties in Table 3. The time histories for each void shape and method are in Figs.41-43 for the elliptical void, the circular void, and the square-shaped void.

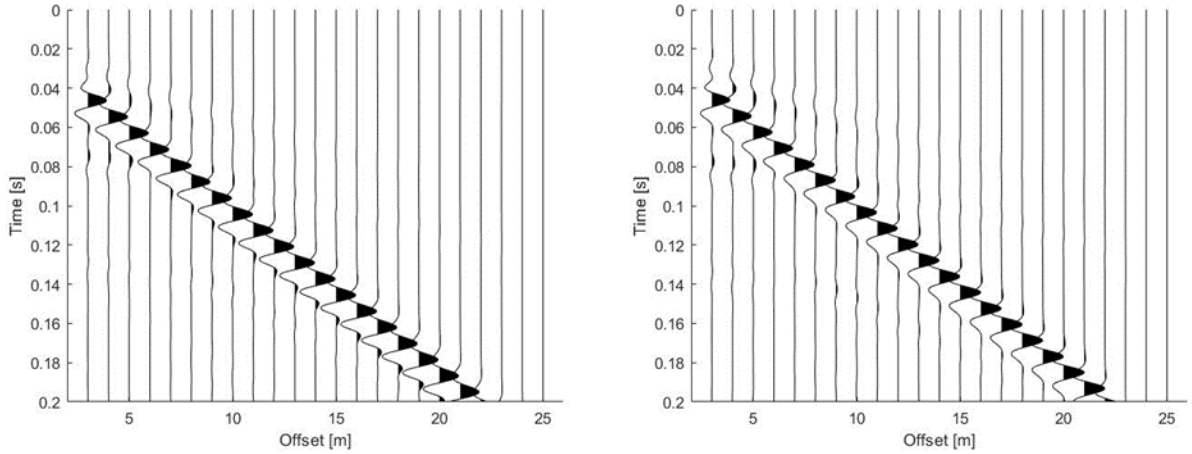

(a) (b)

Figure 41. Surface time history of vertical particle velocity with elliptical void using FDM (a) and FEM (b) in soil.

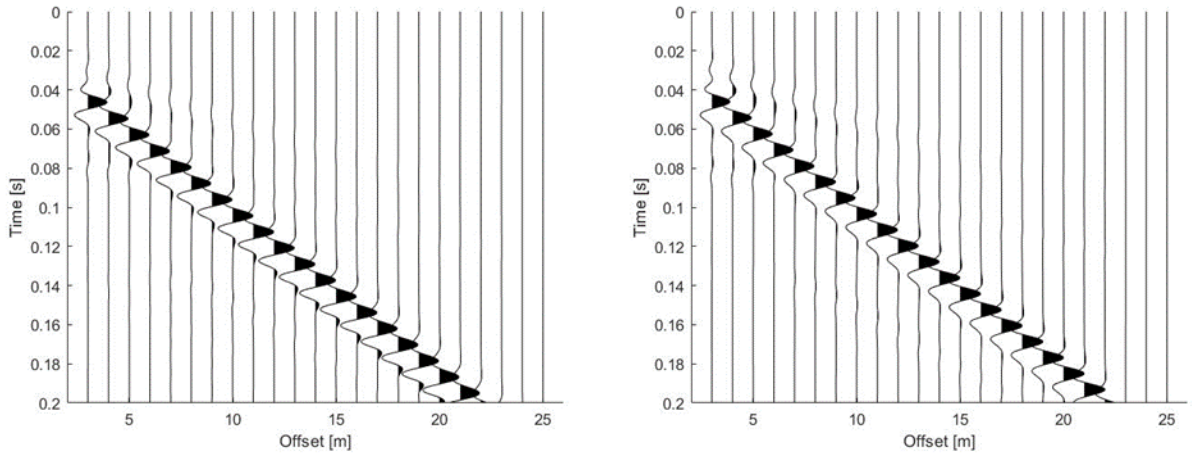

(a) (b)

Figure 42. Surface time history of vertical particle velocity with a circular void using FDM (a) and FEM (b) in soil.

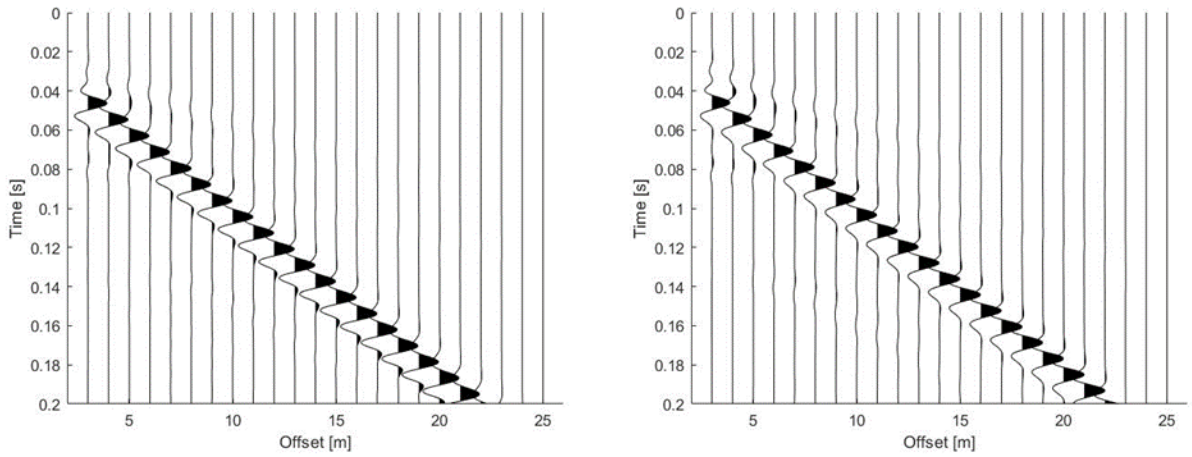

(a) (b)

Figure 43. Surface time history of vertical particle velocity with a square-shaped void using FDM (a) and FEM (b) in soil.

The first reflection seen in the seismograms was between 0.06s and 0.1s from 3m-5m which is in good agreement with the calculated predicted time of 0.0821s. Same as the results in a rock medium, the reflections with the elliptical void are more noticeable than the other void types. The difference was taken from the no-void and void case in the same manner as the rock medium. Figure 44 are the results for the FDM and Fig.45 are for the FEM. From the FDM results, each void was found to have a maximum difference at the 3m receiver, which was 0.0184m/s, 0.0124m/s, and 0.0108m/s for the elliptical void, square void, and circular void, respectively. From the maximum values, it can be said that voids placed in soil have a more significant effect on wave propagation when compared to rock. From the FEM results, the largest difference occurred at the receiver located at 3m and has a value of 0.0085m/s with the elliptical void, 0.0057m/s with the square void, and 0.0049m/s with the circular void. The voids placed in the soil generated a larger difference when compared to rock.

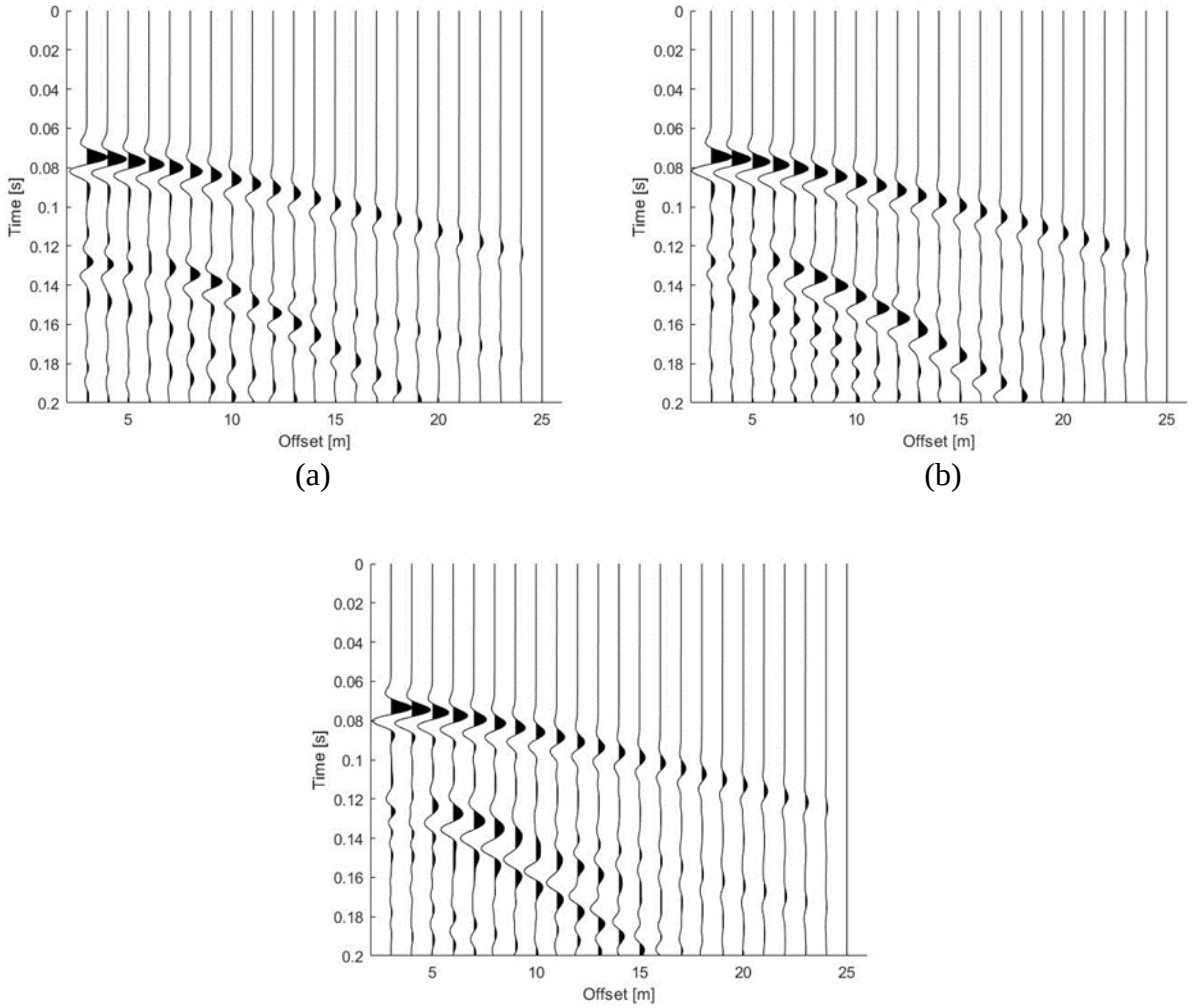

Figure 44. The subtracted vertical particle velocity in the case of the void from the case without void for an elliptical (a), circular (b), and square (c) void in soil using FDM.

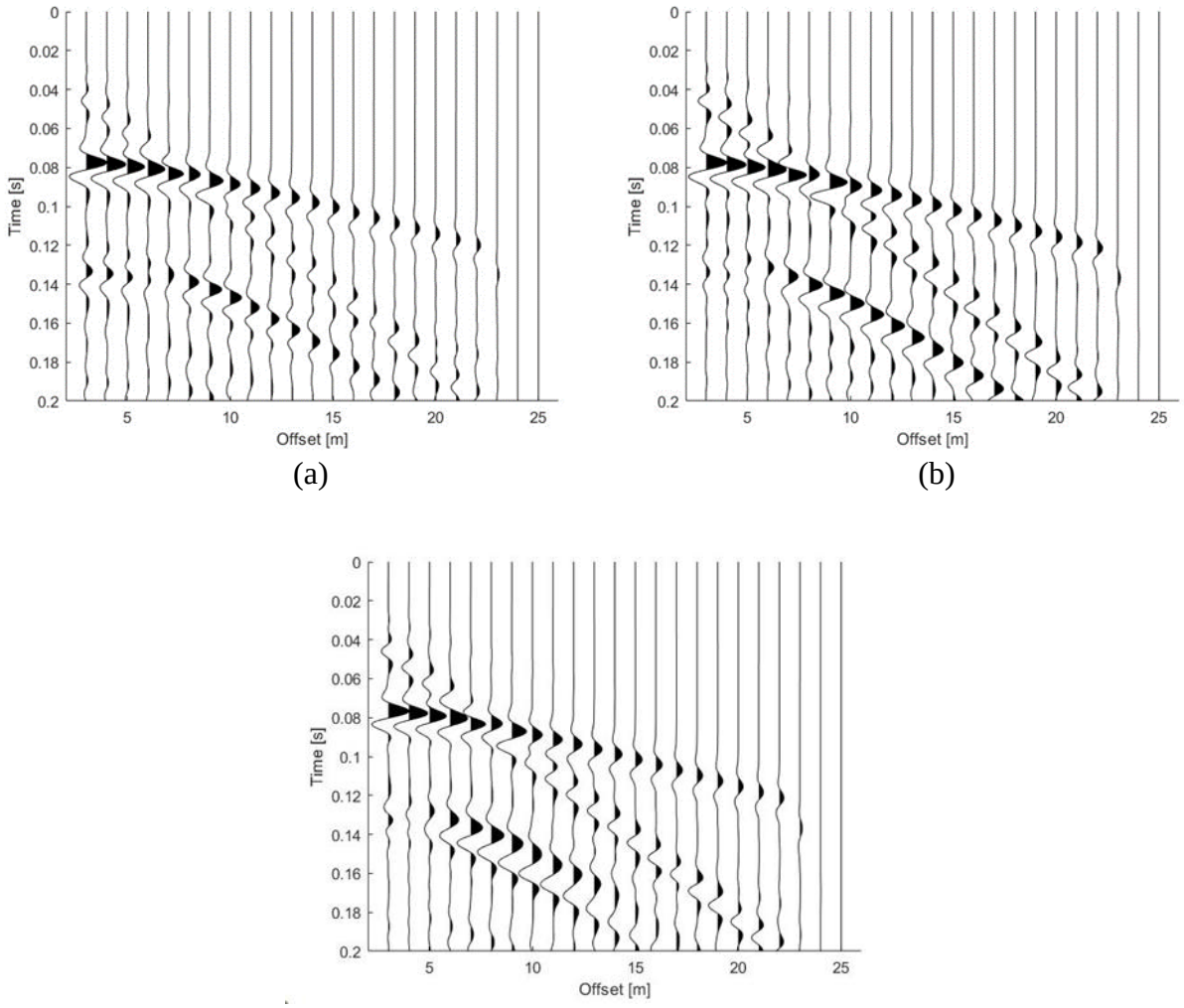

Figure 45. The subtracted vertical particle velocity in the case of the void from the case without void for an elliptical (a), circular (b), and square (c) void in soil using FEM.

4.3 2-D Wave Propagation in a Four-Layered Domain with a Void

A four-layered domain was created, and three different void shapes are placed at the center of the domain, inside the third layer of the domain (see Fig.46). The contour of vertical particle velocity at different points in time in this layered domain with the presence of a circular void using FDM are shown in Fig.47. The range of Fig.47 was purposely lessened to better view the wave propagation. In Fig.47b, the P-wave that has been transmitted through the first two layers can be

seen interacting with the void. The time history of vertical particle velocity of each void case is in Fig.48 for the FDM and Fig.49 for the FEM. There are reflections seen at 0.015s that were not seen in the no void case. Due to reflections from the interfaces in the layered domain, it is challenging to find the location of the void. Therefore, Fig.50 (FDM) and Fig.51 (FEM) were generated by subtracting the data obtained in the case without a void from the case with a void to obtain more information of the effect the void has in the domain.

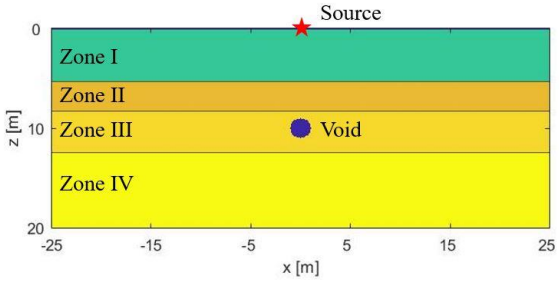

Figure 46. A four-layered domain from results of ultrasonic tests with a void in zone III.

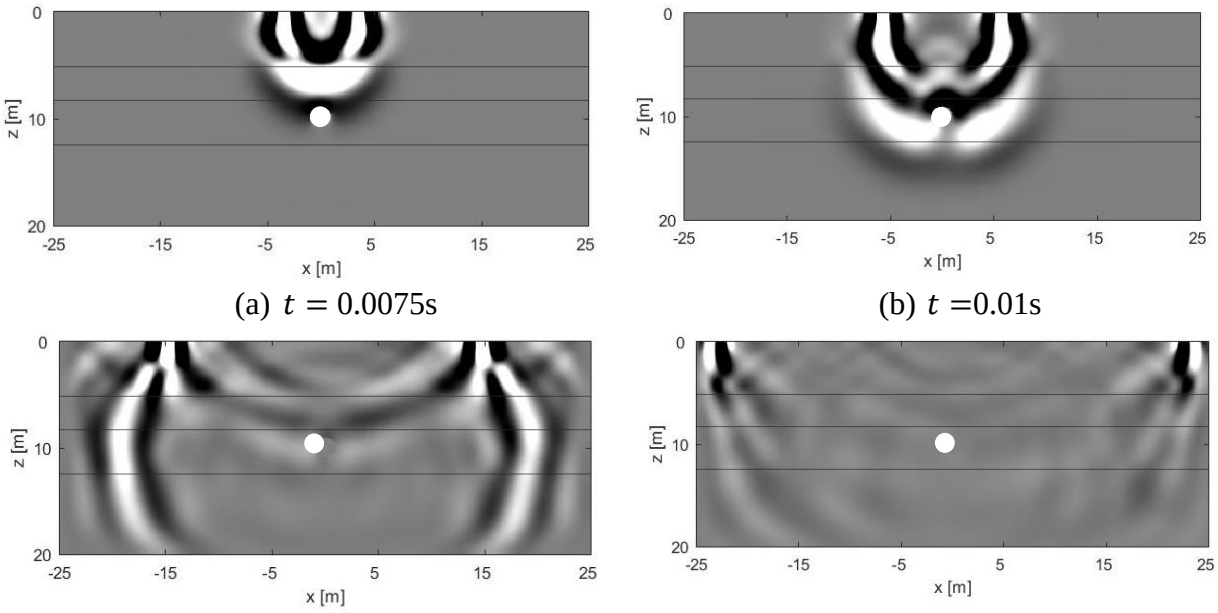

(a) $t = 0.0075$s (b) $t = 0.01$s

(c) $t = 0.02$s (d) $t = 0.03$s

Figure 47. The contour of vertical particle velocity in the case of a circular void at a different time using FDM.

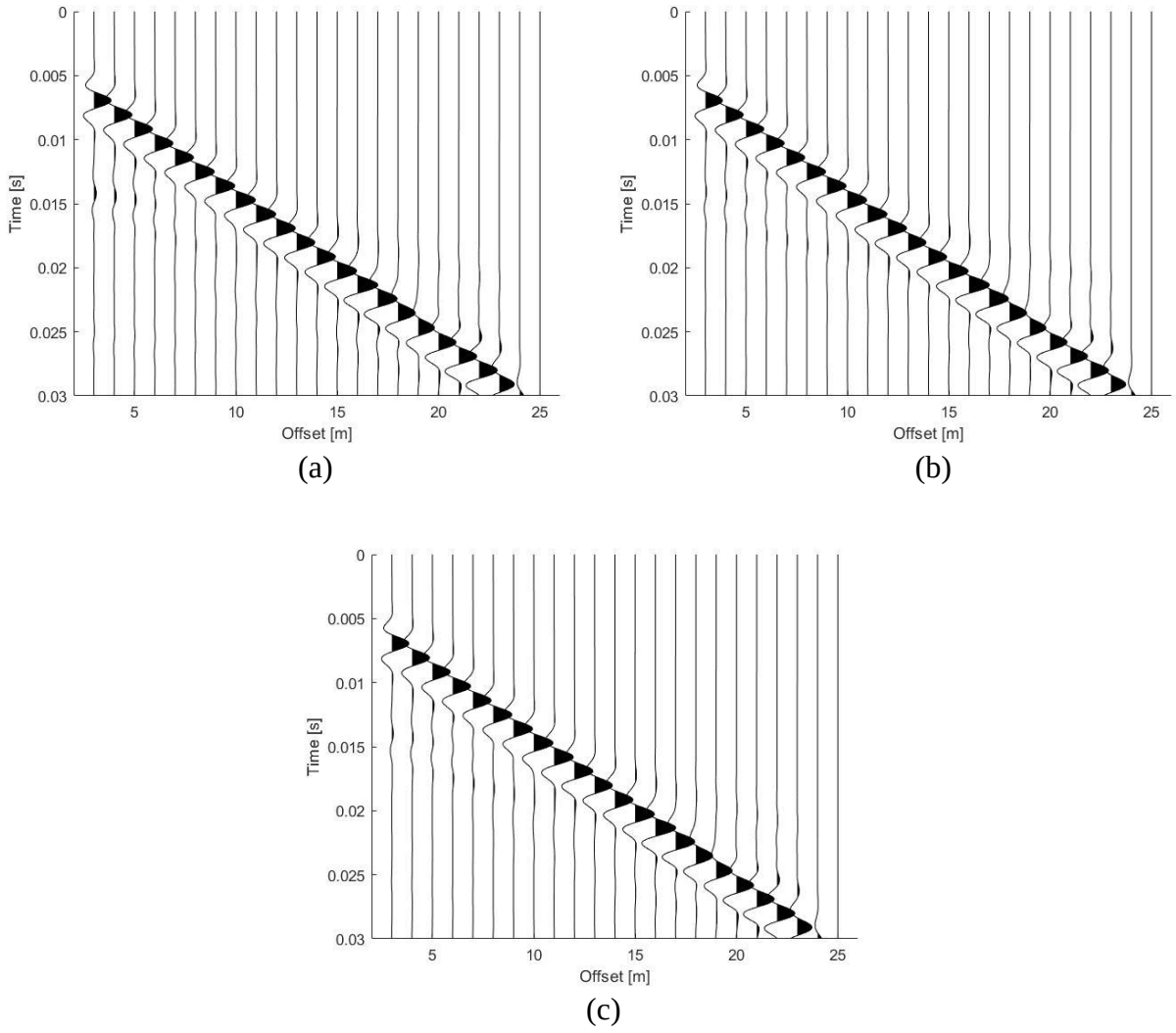

Figure 48. Surface time history of vertical particle velocity with an elliptical (a), circular (b), and square (c) void in a four-layered domain using FDM.

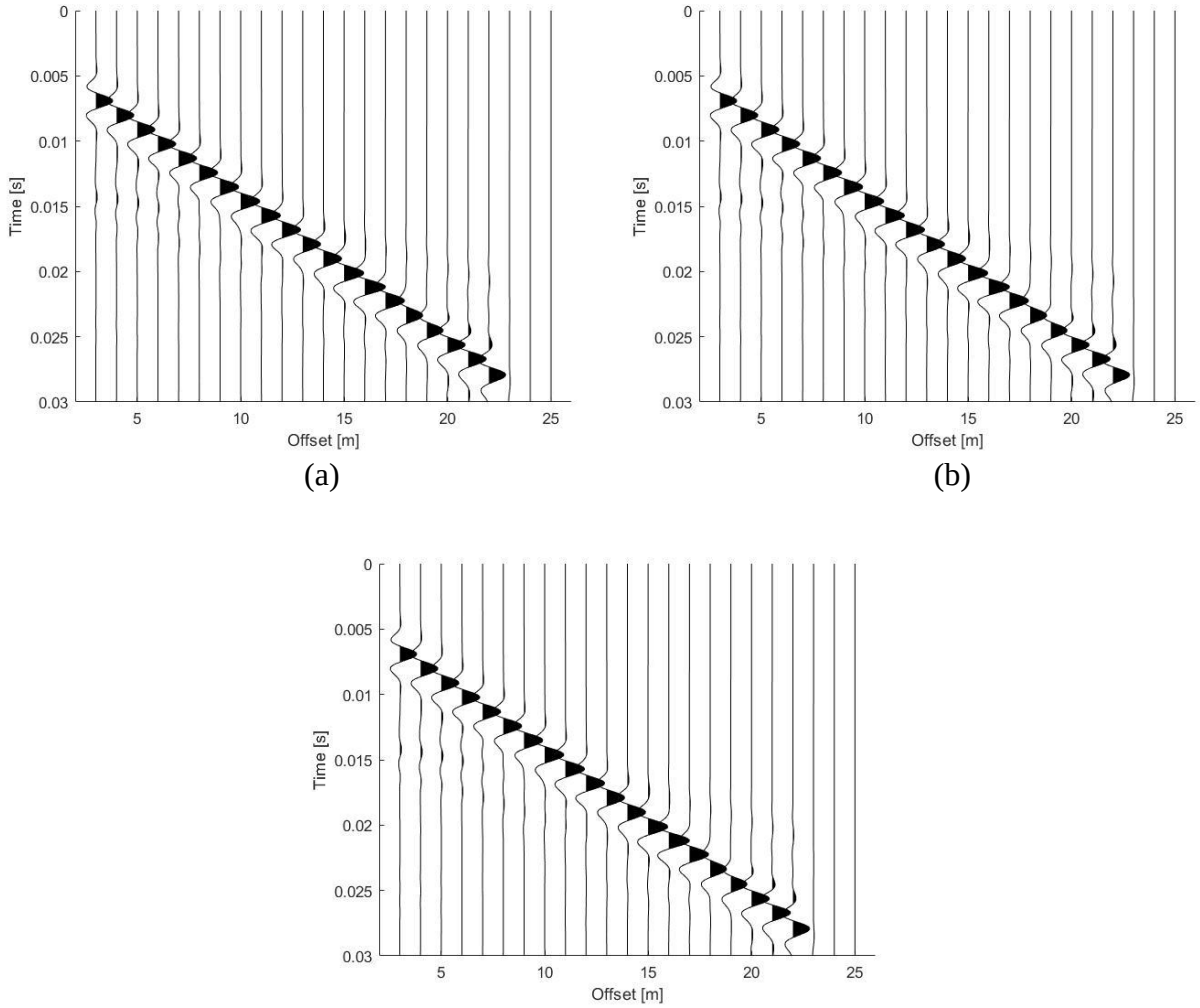

Figure 49. Surface time history of vertical particle velocity with an elliptical (a), circular (b), and square (c) void in a four-layered domain using FEM.

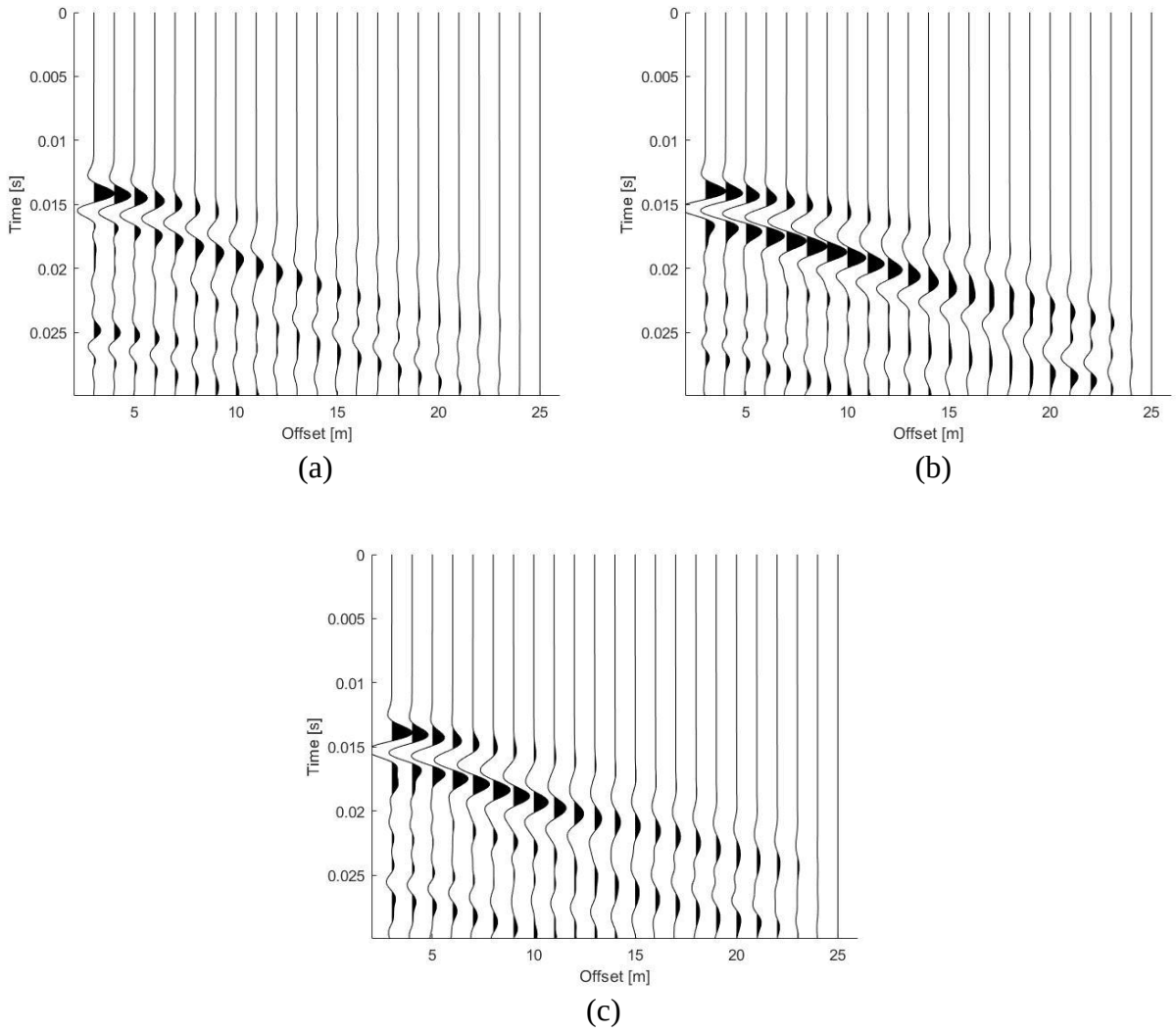

Figure 50. The subtracted vertical particle velocity in the case of the void from the case without void for an elliptical (a), circular (b), and square (c) void in a four-layered domain using FDM.

The elliptical void produced the largest difference of 0.0018m/s followed by the square void at 0.0015m/s and circular void at 0.0012m/s located on the 3m receiver for the FDM. This followed the trend seen in the other media types. For the FEM, the elliptical void had a maximum difference of 0.0020m/s, the square-shaped void was 0.0013m/s and the circular void was 0.0010m/s. Also, the largest difference occurs at 0.015 s, which corresponds to the reflection visible in the surface seismograms in Figs.48-49.

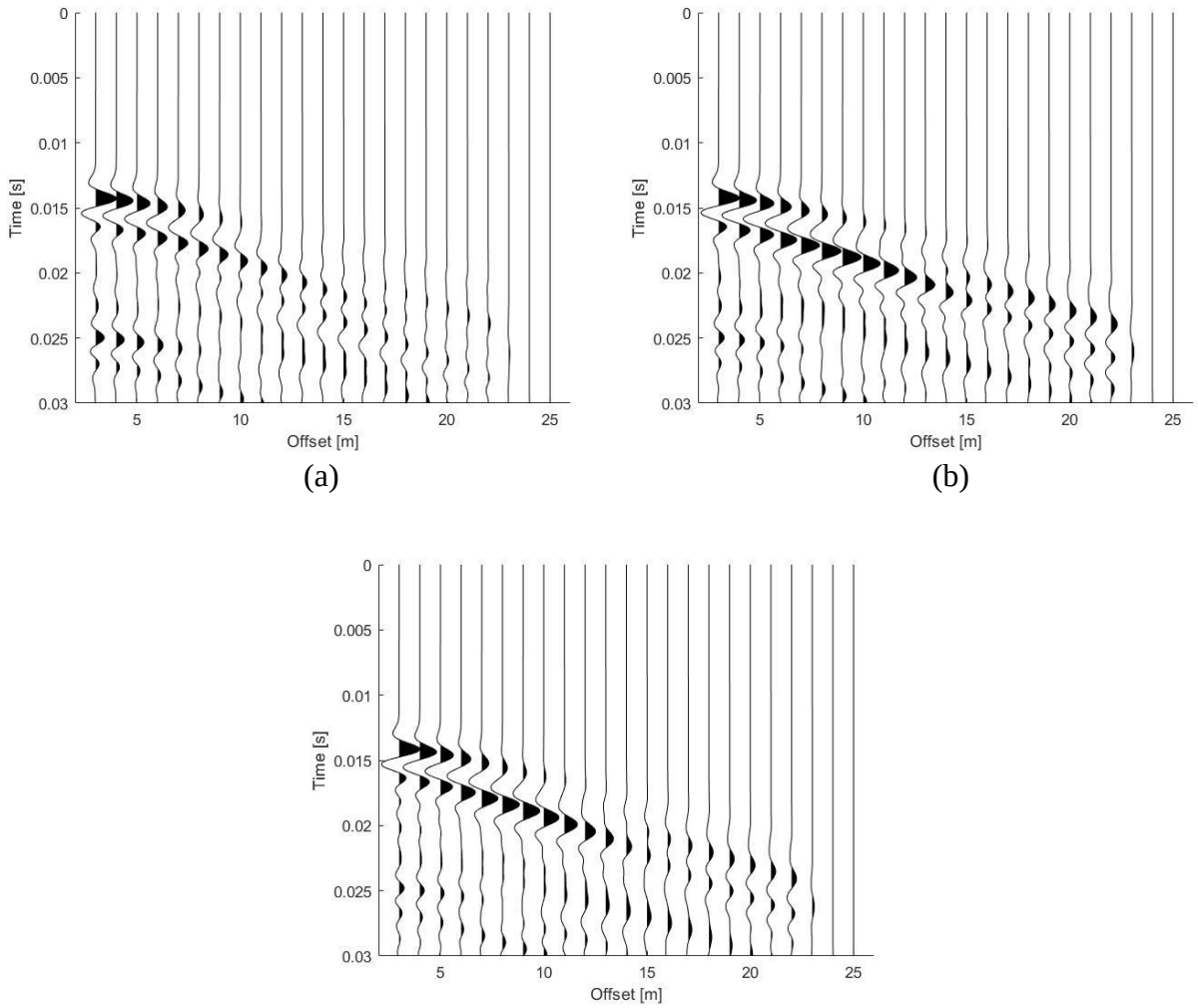

Figure 51. The subtracted vertical particle velocity in the case of the void from the case without void for an elliptical (a), circular (b), and square (c) void in a four-layered domain using FEM.

Different source frequencies were evaluated with the FDM, and their corresponding maximum difference that the subtracted vertical particle velocity displayed is in Fig.52. For the frequencies analyzed, it appeared that there is no general trend on the maximum difference of particle vertical velocity.

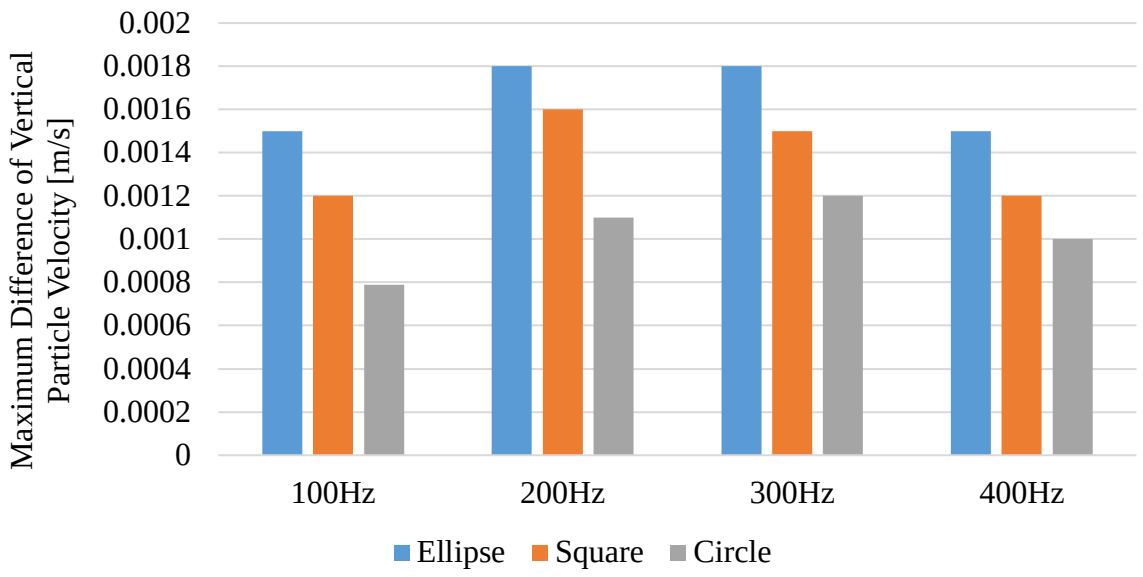

Figure 52. Comparison of the maximum difference of vertical particle velocity at varying frequencies with tested void shapes using FDM.

4.4 2-D Wave Propagation in a Three-Layered Domain with a Void

A void was placed in the center of the three-layered domain analyzed in Section 3.2.3, which featured layers with harsher differences in material properties. All void shapes produced similar surface time histories with each method and visually was difficult to determine the voids influence on the wave propagation. Fig.53 displays the results of the FEM with a circular void compared to its no-void counterpart. All of the resulting surface time histories with each method appeared identical to Fig.53, so only this case was reported. To further analyze the effect each void had, the void case was subtracted from the no void case. Figure 54 reports the subtracted results obtained from the FDM and Fig.55 for the FEM.

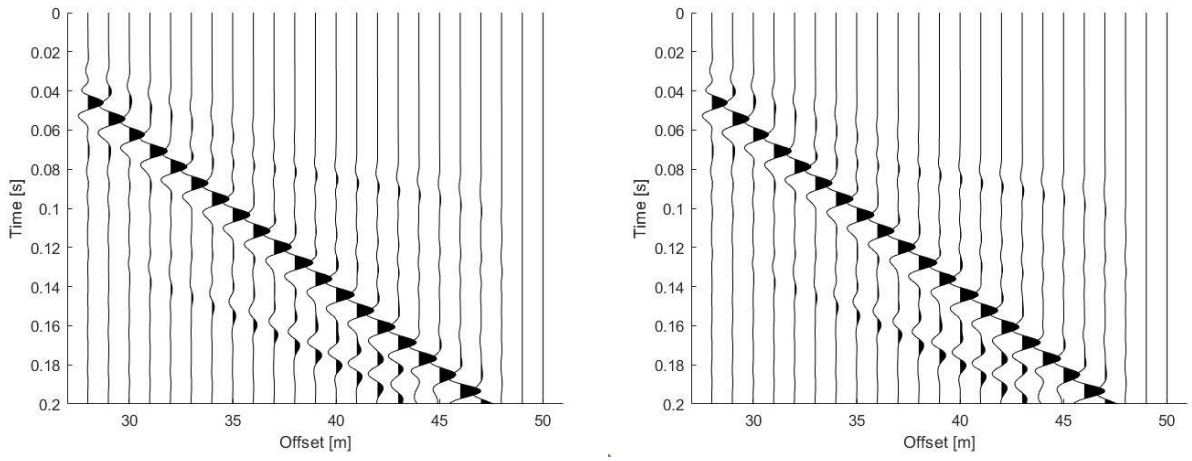

Figure 53. Surface time history of vertical particle velocity without (a) and with (b) a circular void using FEM (a) in a three-layered domain.

From Fig.54, it can be said that the void did influence the wave propagation through the layered domain. The difference between the two seismograms decreased when farther away from the void. The maximum difference occurred at the first receiver location (3m) with an amplitude of 0.0027 m/s, 0.0037 m/s, 0.0040 m/s for the circular void, square void, and elliptical void, respectively, which suggested that the elliptical void had the largest effect on wave propagation. As seen in Fig.55, the void affected the wave propagation, however the results are significantly different from those obtained using FDM. It appears that the maximum amplitude occurred at 22m, however this is the location of the absorbing boundary. Disregarding that point, the maximum amplitude occurred at the receiver at 3m with an amplitude of 0.0025 m/s, 0.0025 m/s, and 0.0031 m/s for the circular void, square void, and elliptical void, respectively.

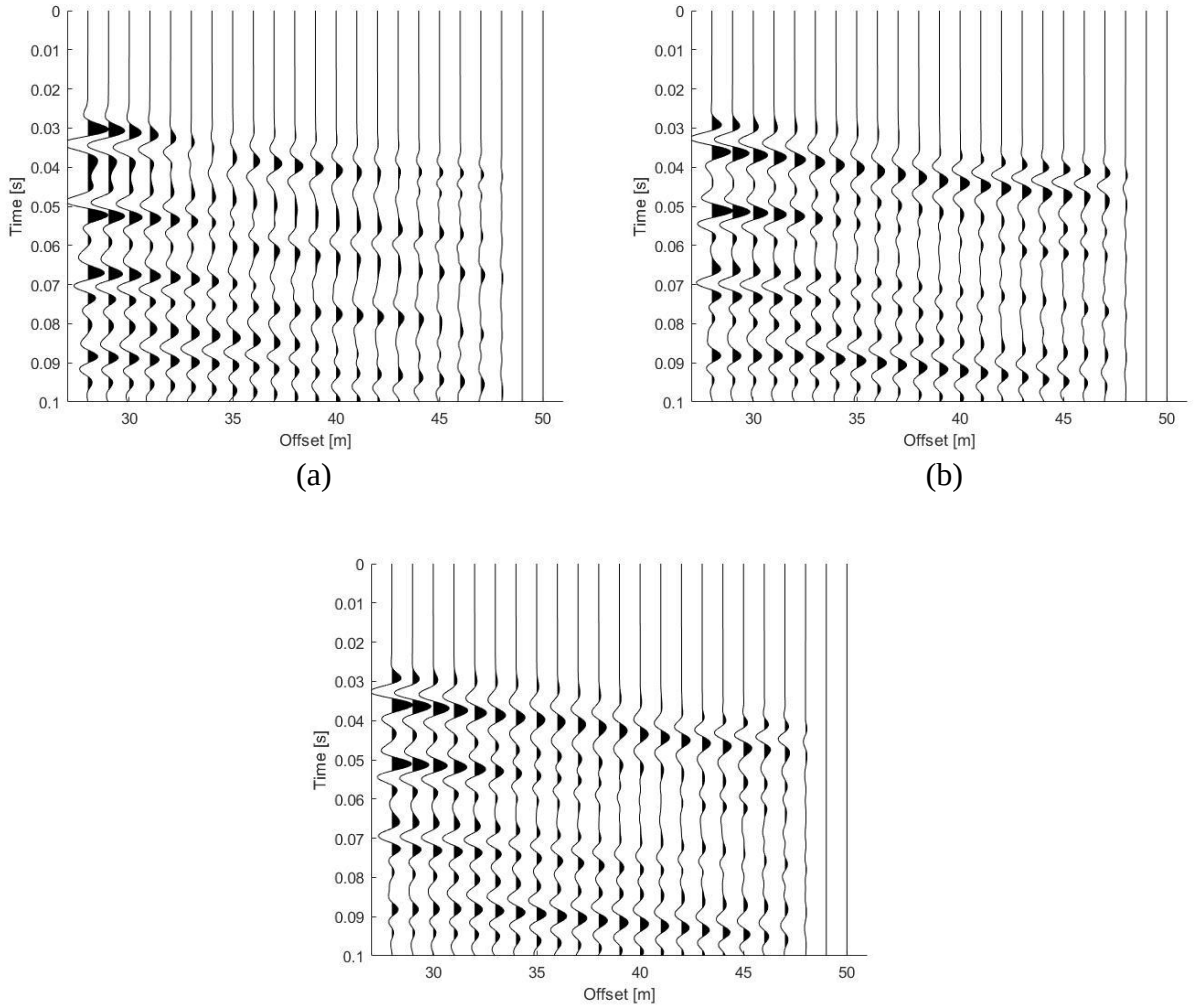

(a) (b)

(c)

Figure 54. The subtracted vertical particle velocity in the case of the void from the case without void for an elliptical (a), circular (b), and square (c) void in a three-layered domain using FDM.

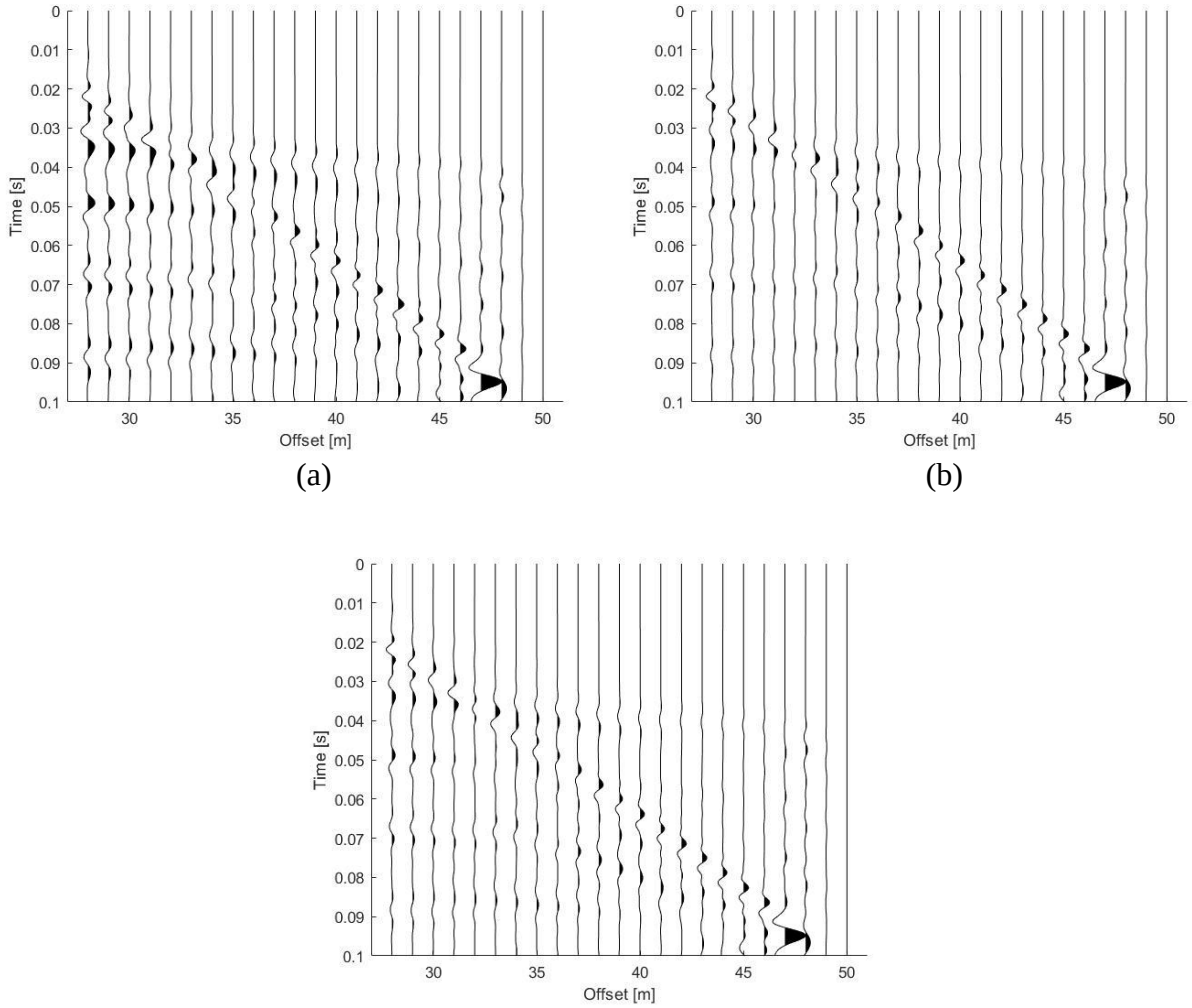

Figure 55. The subtracted vertical particle velocity in the case of the void from the case without void for an elliptical (a), circular (b), and square (c) void in a three-layered domain using FEM.

4.5 Computational Cost and Implementation

Computationally, FDM has shorter simulation times than FEM, with similar times as reported in Table 6 for the no-void cases. While a staircase approximation is used for the circular and elliptical void in the FDM, it did not affect the resulting time histories, but slight noise was reported around the boundary of these void shapes. It was simpler to implement void shapes in the FEM and display cleaner results near the void interface.

Chapter 5: Conclusions and Future Work

The FDM and FEM were compared for 1-D and 2-D elastic wave propagation. In 1-D, a second order in time and space central differencing technique was used for the FDM and the Galerkin formation was used for the FEM. Both methods produced identical results for homogenous wave propagation with varying Courant numbers and source frequencies. Keeping the spatial step the same, a source with a higher frequency produced more dispersion. If a larger frequency is needed, a smaller spatial step will be needed in each method. For layered cases, the Courant number will no longer be 1 in the entire domain, so dispersion occurs in the section that does not exhibit that number. This was more apparent at higher loading frequencies.

For 2-D wave propagation, the staggered grid FDM was used and the discontinuous Galerkin method was used in COMSOL for the FEM. First, homogenous wave propagation was analyzed in rock and soil domains. Both methods produced comparable results in terms of snapshots of the wavefield and surface time histories, where FDM had minimal visible dispersion. Computationally, the FDM had better computational times with the models. Next, ultrasonic testing was conducted to create a more realistic Earth model. A four-layered domain was modeled from the results of the testing, and the resulting seismograms had reflections, but were difficult to notice because the properties were alike and allowed for the waves to travel through the domain easily. A three-layered domain was then modeled that featured a silty clay upper layer and two rock layers. The waves appeared to remain in the first layer and reflections were more visible on the seismograms compared to the four-layered case because of the harsh difference in material properties between the interfaces.

Finally, three void shapes (circle, ellipse, square) were placed in the center of the domains previously studied. Reflections were seen in the time histories for both the rock and soil domains,

where the elliptical void displayed higher amplitude reflections when compared to the other shapes. This is because the elliptical void was longer lengthwise than the other shapes. Computationally, it was simpler to implement voids using the FE software, whereas the FDM suffered from having a stair-case approximation, however, this approximation did not change the outcome of the time histories. Minimal noise could be seen around the outline of the shape as seen in the snapshots of the wavefield. Each void was then analyzed in the four-layered domain. The values obtained from ultrasonic testing were incorporated into the numerical methods. Since the layers shared similar properties, reflections from the voids were slightly visible in the time history seismograms. The results showed that the elliptical void had the largest effect on wave propagation compared to the other void shapes analyzed. This model served as a more realistic subsurface since the samples were prepared from a local site. Different frequencies were analyzed with the FDM and displayed that there was no trend in source frequency and maximum difference of particle vertical velocity with the frequencies assessed. Lastly, the three-layered domain was analyzed with the void shapes. It was difficult to analyze the void's effect on wave propagation by investigating the recorded time histories, so to further study, the difference was taken between the case with a void and the one without a void, and it was found that the void did affect the wave propagation. The elliptical void generated the largest difference. The difference plots from each method varied, where this was attributed to the different source incorporations, however, future work is required to fully analyze why each method produces these results.

In the future, the FEM should be compared to other FD methods such as a higher-order staggered grid and the rotated-staggered grid, which would likely better capture the void's shape. Additionally, more complex models should be compared, for instance, a model with unique topology and non-planar layers to better simulate the Earth's subsurface. Lastly, data analysis

techniques should be applied to the different time history plots to better understand how a void affects wave propagation.

References

[1] Mari, J.L. and Mendes, M., 2019, "Wave propagation," Seismic Imaging: a Practical Approach. Les Ulis: EDP Sciences, pp. 17-34. https://doi.org/10.1051/978-2-7598-2351-2.

[2] Jacobsson, L. and G. Kjell, 2017, "Measurement of p- and s- wave velocity in material using ultrasonics," RISE Report 2017:48.

[3] Marfurt, K.J., 1985, "Accuracy of finite-difference and finite element modeling of the scaler and elastic wave equations," *Geophysics* 49(5): 533-549. https://doi.org/10.1190/1.1441689.

[4] Alterman, Z. and Karal F.C., 1968, "Propagation of elastic waves in layered media by finite-difference methods*," Bulletin of the Seismological Society of America* 58: 367-398. https://doi.org/10.1785/BSSA0580010367.

[5] Boore, D., 1972, "Finite-difference methods for seismic wave propagation in heterogeneous materials," *Methods in Computational Physics* 11. https://doi.org/10.1016/B978-0-12-460811-5.50006-4.

[6] Kelly, K.R., Ward, R.W., Treitel, S., Alford, R.M., 1976, "Synthetic seismograms: a finite-difference approach," *Geophysics* 41(1): 2-27. https://doi.org/10.1190/1.1440605.

[7] Moczo, P., Robertsson, J.O.A., Eisner, L., 2007, "The finite-difference time-domain method for modeling of seismic wave propagation," *Advances in Geophysics* 48: 421–516. https://doi.org/10.1016/S0065-2687(06)48008-0.

[8] Virieux, J., 1984, "SH-wave propagation in heterogeneous media: velocity-stress finite-difference method," *Geophysics* 49: 1933-1957. https://doi.org/10.1190/1.1441605.

[9] Virieux, J., 1986, "P-SV wave propagation in heterogeneous media: velocity-stress finite-difference method," *Geophysics* 51: 889-901. https://doi.org/10.1190/1.1442147.

[10] Levander A.R., 1988, "Fourth-order finite-difference P-SV seismograms," *Geophysics* 53: 1425-1436. https://doi.org/10.1190/1.1442422.

[11] Randall, C.J., 1989, "Absorbing boundary condition for the elastic wave equation: velocity-stress formulation," *Geophysics* 54: 1141-1152. https://doi.org/10.1190/1.1442749.

[12] Yomogida, K. and Etgen, J.T., 1993, "3-D wave propagation in the Los Angeles Basin for the Whittier-Narrows earthquake," *Bulletin of the Seismological Society of America* 83(5): 1325-1344. https://doi.org/10.1785/BSSA0830051325.

[13] Hestholm, S. and Ruud, B., 1994, "2D finite-difference elastic wave modeling including surface topography," *Geophysical Prospecting* 42(5): 371–390. https://doi.org/10.1111/j.1365-2478.1994.tb00216.x.

[14] Hestholm, S. and Ruud, B., 1998, "3-D finite-difference elastic wave modeling including surface topography," *Geophysics* 63(2): 613–622. https://doi.org/10.1190/1.1444360.

[15] Hestholm, S. and Ruud, B., 2001, "2D surface topography boundary conditions in seismic wave modelling," *Geophysical Prospecting* 49(4): 445–460. https://doi.org/10.1046/j.1365-2478.2001.00268.x.

[16] Graves, R.W., 1996, "Simulating Seismic Wave Propagation in 3D Elastic Media Using Staggered-Grid Finite Differences," *Bulletin of the Seismological Society of America* 86(4): 1091-1106. https://doi.org/10.1785/BSSA0860041091.

[17] Bohlen, T. and Saenger E.H., 2006, "Accuracy of heterogenous staggered-grid finite difference modeling of Rayleigh waves," *Geophysics* 71(4): 109-115. https://doi.org/10.1190/1.2213051.

[18] Solano, C.A.P., Donno, D., Chauris, H., 2016, "Finite-difference strategy for elastic wave modelling on curved staggered grid," *Computational Geosciences* 20: 245-264. https://doi.org/10.1007/s10596-016-9561-8.

[19] Mozco, P., Robertsson, J.O.A., Eisner, L., 2007, "The Finite-Difference Time-Domain Method for Modeling of Seismic Wave Propagation," *Advances in Geophysics* 48 (8): 421-516. https://doi.org/10.1016/S0065-2687(06)48008-0.

[20] Virieux, J., Calandra, H., Plessix, R.E., 2011, "A review of the spectral, pseudospectral, finite difference and finite element modelling techniques for geophysical imaging," *Geophysical Prospecting* 59(5): 794-813. https://doi.org/10.1111/j.1365-2478.2011.00967.x.

[21] Cohen, G., Joly, P., Roberts, J.E., Tordjman, N., 2001, "Higher order triangular finite elements with mass lumping for the wave equation," *SIAM Journal on Numerical Analysis* 38(6): 2047–2078. https://doi.org/10.1137/S0036142997329554.

[22] Givoli, D., Hagstrom, T., Patlashenko, I., 2006, "Finite element formulation with high-order absorbing boundary conditions for time-dependent waves," *Computer Methods in Applied Mechanics and Engineering* 195(29-32): 3666–3690. https://doi.org/10.1016/j.cma.2005.01.021.

[23] Givoli, D. and Neta, B., 2003, "High-order non-reflecting boundary scheme for time-dependent waves," *Journal of Computational Physics* 186(1): 24–46. https://doi.org/10.1016/S0021-9991(03)00005-6.

[24] Lysmer, J. and Drake, L.A., 1972, "A Finite Element Method for Seismology," *Methods in Computational Physics: Advances in Research and Applications* 11: 181-216. https://doi.org/10.1016/B978-0-12-460811-5.50009-X.

[25] Seron, F.J., Sanz, F.J., Kindelan, M., Badal, J.I., 1990, "Finite Element Method for Elastic Wave Propagation," *Communications in Applied Numerical Methods* 6(5): 359-368. https://doi.org/10.1002/cnm.1630060505.

[26] Toshinawa, T. and Ohmachi, T., 1992, "Love-wave propagation in a three-dimensional sedimentary basin," *Bulletin of the Seismological Society of America* 82(4): 1661–1677. https://doi.org/10.1785/BSSA0820041661.

[27] Ham, S. and Bathe, K.J., 2012, "A finite element method enriched for wave propagation problems," *Computers and Structures* 94-95: 1-12. https://doi.org/10.1016/j.compstruc.2012.01.001.

[28] Liu, G.R. and Nguyen, T.T., 2010, *Smoothed Finite Element Method*, CRC Press, New York, NY.

[29] Wang, G., Cui X.Y., Feng, H., and Li, G.Y., 2015, "A stable node-based smoothed finite element method for acoustic problems," *Computer Methods in Applied Mechanics and Engineering* 297: 348–370. https://doi.org/10.1016/j.cma.2015.09.005.

[30] Chai, Y., Zhang, Y., 2020, "Transient Wave Propagation Dynamics with Edge-Based Smoothed Finite Element Method and Bathe Time Integration Technique," *Mathematical Problems in Engineering* 2020: 1-16. https://doi.org/10.1155/2020/7180489.

[31] Gelis, C., Laparoux, D., Virieux, J., Bitri, A., Operto, S., Grandjean, G., 2005, "Numerical Modeling of Surface Waves Over Shallow Cavities," *Journal of Environmental and Engineering Geophysics* 10(2): 111-121. https://doi.org/10.2113/JEEG10.2.111

[32] Schroder C.T. and Scott, W.R., 2000, "A Finite-Difference Model to Study the Elastic-Wave Interactions with Buried Land Mines," *IEEE Transactions on Geoscience and Remote Sensing* 38(4): 1505-1512. https://doi.org/10.1109/36.851950.

[33] Jianghai, X., Nyquist, J.E., Xu, Y., Roth, M.J.S., Miller, R.D., 2007, "Feasibility of detecting near-surface feature with Rayleigh-wave diffraction," *Journal of Applied Geophysics* 62(3)" 244-253. https://doi.org/10.1016/j.jappgeo.2006.12.002.

[34] Zeng, C., Xia, J., Miller, R.D., 2009, "Modeling results on detectability of shallow tunnels using Rayleigh-wave diffraction," *SEG Technical Program Expanded Abstracts*, 1425-1429. https://doi.org/10.1190/1.3255116.

[35] Mirassi, S. and Rahnema, H., 2020, "Deep cavity detection using propagation of seismic waves in homogenous half-space and layered soil media," *Asian Journal of Civil Engineering* 21: 1431–1441. https://doi.org/10.1007/s42107-020-00288-2.

[36] Basu, A. and Aydin, A., 2005, "Evaluation of Ultrasonic Testing in Rock Material Characterization," *Geotechnical Testing Journal* 29(2): 117-125. http://dx.doi.org/10.1520/GTJ12652.

[37] Faim, R., Andrade, P., Figueiredo, F., 2015, "Physical and mechanical characterization of dolomitic limestone in Coimbra (Central Portugal)," Future Development of Rock Mechanics, Austrian Society of Geomechanics, pp.547-551.

[38] Rahmouni, A., Boulanouar, A., Boukalouch, M., Géraud, Y., Samaouali, A., Harnafi, M., Sebbani, J., 2013, "Prediction of Porosity and Density of Calcarenite Rocks from P-Wave Velocity Measurements," *International Journal of Geosciences* 4(9): 1292-1299. http://dx.doi.org/10.4236/ijg.2013.49124.

[39] Langtangen, H.P., 2016, *A Primer on Scientific Programming with Python*, Springer Berlin Heidelberg.

[40] COMSOL Multiphysics® v. 6.1. www.comsol.com. COMSOL AB, Stockholm, Sweden.

[41] Cerjan, C., Kosloff, D., Kosloff, R., Reshef M., 1985, "A nonreflecting boundary condition for discrete acoustic and elastic wave equations," *Geophysics* 50(4): 705-708. https://doi.org/10.1190/1.1441945.

[42] Berenger, J.P., 1994, "A perfectly matched layer for the absorption of electromagnetic waves," *Journal of Computational Physics* 114(2): 185–200. https://doi.org/10.1006/jcph.1994.1159.

[43] Chew, W.C. and Liu, Q.H., 1996, "Perfectly matched layers for elastodynamics: A new absorbing boundary condition," *Journal of Computational Acoustics* 4(4): 72–79. https://doi.org/10.1142/S0218396X96000118.

[44] Zeng, C., Xia, J., Miller, R.D., Tsoflias, G.P., 2012, "An improved vacuum formation formulation for 2D finite-difference modeling of Rayleigh waves including surface topography and internal discontinuities," *Geophysics* 77(1): T1-T9. https://doi.org/10.1190/geo2011-0067.1.

[45] Mittet, R., 2002, "Free-surface boundary conditions for elastic staggered-grid modeling schemes," *Geophysics* 67(5): 1616-1623. https://doi.org/10.1190/1.1512752.

[46] DeBasabe, J.D. and Sen, M.K., 2015, "A comparison of finite-difference and spectral-element methods for elastic wave propagation in media with a fluid-solid interface," *Geophysical Journal International* 200(1): 278-298. https://doi.org/10.1093/gji/ggu389.

Appendix A: IRB Letter Approval

MARSHALL UNIVERSITY
www.marshall.edu

Office of Research Integrity

March 6, 2023

Brittany Ballengee
3057 Wilson Road
Barboursville, WV 25504

Dear Brittany,

This letter is in response to the submitted thesis abstract entitled *"The Simulation of Elastic Wave Propagation in Presence of Void in the Subsurface."* After assessing the abstract, it has been deemed not to be human subject research and therefore exempt from oversight of the Marshall University Institutional Review Board (IRB). The Code of Federal Regulations (45CFR46) has set forth the criteria utilized in making this determination. Since the information in this study does not involve human subjects as defined in the above referenced instruction, it is not considered human subject research. If there are any changes to the abstract, you provided then you would need to resubmit that information to the Office of Research Integrity for review and a determination.

I appreciate your willingness to submit the abstract for determination. Please feel free to contact the Office of Research Integrity if you have any questions regarding future protocols that may require IRB review.

Sincerely,

Bruce F. Day, ThD, CIP
Director

Appendix B: Staggered Grid Finite Difference Code

```
%% Staggered Grid FDM Code
% Brittany Ballengee
% Marshall University : College of Engineering and Computer Sciences

%% Setup
clc
clear

lx=50;   % Horizontal Length
lz=20;   % Vertical Length
dx=0.1;  % Step Size
dz=dx;
nx=floor(lx/dx+1);
nz=floor(lz/dz+1);

% Material Properties
vp=2700*ones(nz,nx); % Solid layer P-velocity
vs=1400*ones(nz,nx); % Solid layer S-velocity
rho=1200*ones(nz,nx);% Solid Density


% Coordinates
for i=1:nx
      x_cor(i)=dx*(i-1);
end

for k=1:nz
     z_cor(k)=dz*(k-1);
end

% Center
x_cent=dx*(round(nx/2)-1);
z_cent=dz*(round(nz/2)-1);

% Vacuum Formation
vp(1:5,1:end)=0;
vs(1:5,1:end)=0;
rho(1:5,1:end)=0;

%% Trace Location
x_loc=round(nx/2)+3/dx:1/dx:nx; % X-Reciever locations
z_loc=6;
x_loc_real=lx/2+3:1:lx; % Real location, 1m apart
f2=length(x_loc);

%% Multiple Layer Domain

% Comment if not analyzing layers

% Layer 1
vp(3:round(5/dx)+3,1:end)=1449.4; % Depth of first layer was 5 m
vs(3:round(5/dx)+3,1:end)=1057.9;
```

```
rho(3:round(5/dx)+3,1:end)=2608.7;

% Layer 2
vp(round(5/dx)+4:round(8/dx)+4,1:end)=2041.7; % Depth of second layer was 8 m
vs(round(5/dx)+4:round(8/dx)+4,1:end)=1510.6;
rho(round(5/dx)+4:round(8/dx)+4,1:end)=2202.5;

% Layer 3
vp(round(8/dx)+5:round(12/dx)+5,1:end)=2322.0; % Depth of third layer was 12 m
vs(round(8/dx)+5:round(12/dx)+5,1:end)=1650.3;
rho(round(8/dx)+5:round(12/dx)+5,1:end)=2566.5;

% Layer 4
vp(round(12/dx)+6:end,1:end)=2550.7; % Last layer
vs(round(12/dx)+6:end,1:end)=1991.4;
rho(round(12/dx)+6:end,1:end)=2443.55;

%% Void Incorporation

% Have one void shape uncommented and remaining commented if running void cases

% Elliptical Void
for ii=1:nx
   for kk=1:nz
       if(((x_cor(ii)-x_cent)/2)^2+((z_cor(kk)-z_cent)/1)^2<=1)
            rho(round(kk),round(ii))=0; % Density of fluid
            vp(round(kk),round(ii))=0;
            vs(round(kk),round(ii))=0;
       end
   end
end

% Circular Void
% for ii=1:nx
%    for kk=1:nz
%        if(((x_cor(ii)-x_cent)/1)^2+((z_cor(kk)-z_cent)/1)^2<=1)
%             rho(round(kk),round(ii))=0; % Density of fluid
%             vp(round(kk),round(ii))=0;
%             vs(round(kk),round(ii))=0;
%        end
%    end
% end

% Square Void
% l_box=1; % Half-length of square
% w_box=1; % Half-width of square
%
% vp(round(nz/2)-round(w_box/dz):round(nz/2)+round(w_box/dz),round(nx/2)-
round(l_box/dz):round(nx/2)+round(l_box/dz))=0;
%
% vs(round(nz/2)-round(w_box/dz):round(nz/2)+round(w_box/dz),round(nx/2)-
round(l_box/dz):round(nx/2)+round(l_box/dz))=0;
%
% rho(round(nz/2)-round(w_box/dz):round(nz/2)+round(w_box/dz),round(nx/2)-
round(l_box/dz):round(nx/2)+round(l_box/dz))=0;
```

```
%% Addtional Parameters
M=vs.*vs.*rho;  % mu
L=vp.*vp.*rho-2.*M; % lambda
B=1./rho; % Inverse of density

%% Time
T_total=0.03;  % Total time
dt=dx/(max(vp(:))*sqrt(2)); % Time step

nt=round(T_total/dt);
t = 0:dt:T_total;

%% Source Excitation
f0=300; % Source frequency
sx=round(nx/2); % Source x-location
sz=6; % Source z-location
angle_force=0;
t0=1.4*sqrt(6)/(pi*f0);
a2=(pi*f0*(t-t0)).^2;
ricker=(1-2.*a2).*exp(-a2);

plot(t,ricker);
xlabel('Time [s]')
ylabel('Amplitude')

force_x = sin(angle_force * pi / 180) * ricker * dt / (dx * dx * rho(sz,sx));
force_z = cos(angle_force * pi / 180) * ricker * dt / (dx * dx * rho(sz,sx));

%% Absorbing Boundary (ABS)
abs_thick = min(floor(0.15*nx), floor(0.15*nz));         % thicknes of the layer
abs_rate = 0.3/abs_thick;      % decay rate

lmargin = [abs_thick abs_thick];
rmargin = [abs_thick abs_thick];
weights = ones(nz,nx);
for iz = 1:nz
    for ix = 1:nx
        i = 0;
        j = 0;
        k = 0;
       if (ix < lmargin(1) + 1)
           i = lmargin(1) + 1 - ix;
       end
%         if (iz < lmargin(2) + 1)   % Removed from the top boundary (z=0)
%             k = lmargin(2) + 1 - iz;
%         end
        if (nx - rmargin(1) < ix)
            i = ix - nx + rmargin(1);
        end
        if (nz - rmargin(2) < iz)
            k = iz - nz + rmargin(2);
        end
```

```
        if (i == 0 && j == 0 && k == 0)
            continue
        end
        rr = abs_rate * abs_rate * double(i*i + j*j + k*k );
        weights(iz,ix) = exp(-rr);
    end
end
%% Initialization

% Velocity
U1=zeros(nz,nx);
V1=zeros(nz,nx);
U2=zeros(nz,nx);
V2=zeros(nz,nx);


% Stress
Sigma1=zeros(nz,nx);
T1=zeros(nz,nx);
Ksi1=zeros(nz,nx);
Sigma2=zeros(nz,nx);
T2=zeros(nz,nx);
Ksi2=zeros(nz,nx);

for it = 1:nt

    for iz = 2:nz-1
        for ix=2:nx-1
            % U - Velocity
           if rho(iz,ix)==0 && rho(iz,ix+1)==0 % Free Surface
                B(iz,ix)=0;
           else
                B(iz,ix)=2/(rho(iz,ix)+rho(iz,ix+1));
           end
              U2(iz,ix) = U1(iz,ix)+ (B(iz,ix)*dt/dx)*(Sigma1(iz,ix) - Sigma1(iz,ix-
1))+(B(iz,ix)*dt/dz)*(Ksi1(iz,ix) -Ksi1(iz-1,ix));
        end
    end

    for iz = 2:nz-1
        for ix=2:nx-1
            % V- Velocity
            if rho(iz,ix)==0 && rho(iz+1,ix)==0 % Free Surface
                B(iz,ix)=0;
            else
                B(iz,ix)=2/(rho(iz,ix)+rho(iz+1,ix));
            end
             V2(iz,ix) = V1(iz,ix)+ (B(iz,ix)*dt/dx)*(Ksi1(iz,ix+1)-
Ksi1(iz,ix))+(B(iz,ix)*dt/dz)*(T1(iz+1,ix)-T1(iz,ix));
             V2(sz,sx) = V2(sz,sx) + force_z(it); % Velocity source
        end
    end


    for iz = 2:nz-1
```

```
        for ix=2:nx-1
            % Sigma_xx Stress
             Sigma2(iz,ix)= Sigma1(iz,ix)+(L(iz,ix)+2*M(iz,ix)) *
(dt/dx)*(U2(iz,ix+1) - U2(iz,ix))+L(iz,ix)*(dt/dz)*(V2(iz,ix)- V2(iz-1,ix));
        end
    end

    for iz = 2:nz-1
            for ix=2:nx-1
             % Sigma_zz Stress
             T2(iz,ix) = T1(iz,ix)+(L(iz,ix)+2*M(iz,ix)) * (dt/dz) * (V2(iz,ix) -
V2(iz-1,ix))+L(iz,ix) * (dt/dx) * (U2(iz,ix+1)-U2(iz,ix));
            end
    end

    for iz = 2:nz-1
            for ix=2:nx-1
             % Sigma_xz Stress
                if (M(iz,ix)~=0) && (M(iz,ix+1)~=0) && (M(iz+1,ix)~=0) &&
(M(iz+1,ix+1)~=0) % Free Surface
                    Ksi2(iz,ix) = Ksi1(iz,ix)+
(1/4*(1/M(iz,ix)+1/M(iz,ix+1)+1/M(iz+1,ix)+1/M(iz+1,ix+1)))^(-1)* (dt/dz) *
(U2(iz+1,ix) - U2(iz,ix) + V2(iz,ix)- V2(iz,ix-1));
                else
                    Ksi2(iz,ix) = Ksi1(iz,ix)+ 0* (dt/dz) * (U2(iz+1,ix) - U2(iz,ix)
+V2(iz,ix)- V2(iz,ix-1));
                end
             end
     end


    U1=U2.*weights;
    V1=V2.*weights;
    Sigma1=Sigma2.*weights;
    T1=T2.*weights;
    Ksi1=Ksi2.*weights;


     for m=1:f2
         V2_out(it,m)=V2(z_loc,x_loc(m)); % Recording vertical velocity traces
     end

        % Plotting
        if mod(it,25) == 0
        title([' Time: ',sprintf('%.4f',t(it)),' sec']);
        figure(1)
        imagesc(V2)
        colormap gray; xlabel('x [m]'); ylabel('z[m]');
        colorbar
        h = colorbar;
        ylabel(h, 'Vertical Particle Velocity')
        xticklabels = -25:10:25; % Change accordingly to domain size
        xticks = linspace(1, size(V2, 2), numel(xticklabels));
        set(gca, 'XTick', xticks, 'XTickLabel', xticklabels)
        yticklabels = 20:-10:0; % Change accordingly to domain size
```

```
        yticks = linspace(1, size(V2, 1), numel(yticklabels));
        set(gca, 'YTick', yticks, 'YTickLabel', flipud(yticklabels(:)))
        axis equal tight; drawnow;
        frame = getframe(1);

        % Gif Generation
        im = frame2im(frame);
        [imind,cm] = rgb2ind(im,256);
        outfile = '2D_FDM.gif'; % File Title
        if it==25
            imwrite(imind,cm,outfile,'gif','DelayTime',0,'loopcount',inf);
        else
            imwrite(imind,cm,outfile,'gif','DelayTime',0,'writemode','append');
        end
        end
end
%% Trace Plot
figure(2)

x_loc3_real=3:1:25;
wiggle(t,x_loc3_real,V2_out3)
ylabel('Time [s]')
xlabel('Offset [m]')
ylim([0 0.03])
```